Instrumented Footwear to Measure Plantar Tissue Properties

Tony C. Huynh

A thesis submitted
in partial fulfillment of the
requirements for the degree of

Master of Science in Mechanical Engineering

University of Washington
2020

Committee:
William R. Ledoux (chair)
Scott Telfer
Michael Bailey
Nathan Sniadecki

Program Authorized to Offer Degree:
Department of Mechanical Engineering

University of Washington

Abstract

Instrumented Footwear to Measure Plantar Tissue Properties

Tony C. Huynh

Chair of the Supervisory Committee:
Affiliate Professor William R. Ledoux
Departments of Mechanical Engineering and Orthopaedics & Sports Medicine

The prevalence of diabetes is increasing in the United States, and the lack of a cure makes it imperative to manage symptoms to prevent overall health from worsening. Diabetes-related foot complications include peripheral neuropathy and ulceration. Greater understanding of the biomechanical changes to the foot soft tissue can help inform clinicians on better care and also guide the design of diabetic footwear and orthoses. To improve understanding, researchers have conducted various studies on diabetic feet. In vivo studies that used ultrasonography often had test subjects in static positions. In cases where test subjects ambulated, radiography was used to image soft tissue, exposing test subjects to ionization. To overcome these limitations, an instrumented shoe was designed and developed to capture the dynamic properties of plantar soft tissue during gait. The footwear, developed with additive manufacturing in mind, was equipped with a custom ultrasound probe and four load cells, which provided displacement and force data, respectively. The sensors went through validation tests that confirmed accurate data collection. A pilot study was done on a test subject walking on a treadmill. Several trials were conducted to collect data at the heel and forefoot. The displacement and force data were used to create force-

deformation curves to help inform soft tissue deformation, peak force, tissue stiffnesses, and energy dissipation ratio. The data were comparable to the literature. Though the pilot study only used one test subject, the instrumented shoe demonstrated its ability to collect viable data. However, the footwear durability was in question. Improvements to the data collection process and further refinement of the footwear are necessary to make a reliable instrumented footwear.

TABLE OF CONTENTS

LIST OF FIGURES

LIST OF TABLES

ABBREVIATIONS

APL-Applied Physics Laboratory

BW-body weight

CAD-computer-aided design

CAUD-caudal angle

CLiMB-Center for Limb Loss and MoBility

CT-computed tomography

DAQ-data acquisition

DIC-digital image correlation

DICOM-digital imaging and communications in medicine

FDM-fused deposition modeling

FPGA-field programmable gate array

IRB-Institutional Review Board

JPEG-joint photographic experts group

LAO-left anterior oblique angle

LV-LabVIEW

MRI-magnetic resonance imaging

NIH-National Institutes of Health

RAO-right anterior oblique angle

ROI-region of interest

SSI-SuperSonic Imagine

US-ultrasound

UW-University of Washington

VA-Veterans Affairs

ACKNOWLEDGEMENTS

I want to thank everyone who has helped me along my graduate education. I have been challenged throughout my time here and have learned a lot about engineering and biomechanics.

Thank you, Bil and Scott, for your patience and guidance in my thesis.
Thank you, Matt, for sharing so much knowledge and insight.
Thank you, Lynda, for helping me countless times on topics related to ultrasound and beyond.
Thank you, Eric, for helping me learn to use Mimics and sharing your passion in engineering.

To all my friends and family who have supported me nonstop during my time in Seattle-thank you.

Funding for this study was provided by NIH R21 grant AR072216-01.

Chapter 1. INTRODUCTION

1.1 PREVALENCE AND EFFECTS OF DIABETES

Diabetes mellitus is a disease in which the pancreas is impaired. The pancreas releases insulin which allows glucose in the blood to be used by cells. Without the proper amount of insulin, glucose can accumulate in the blood, leading to what many refer to as having a high blood sugar level. The high level of blood sugar can be damaging to the body. The prevalence of diabetes is increasing in America. In 2009, a study estimated that 23.7 million Americans between the ages of 24 and 85 had diabetes; this number was expected to rise to 44.1 million by 2034 [1]. Alongside with the increase in people with diabetes was the increase in diabetic medical costs; in the same time frame, annual costs were expected to rise from $113 billion to $336 billion [1]. A report by the American Diabetes Association in 2017 estimated diabetes-related costs to be $327 billion, of which $237 billion were direct medical costs and the rest being the cost of lost productivity [2]. Certain groups of people are more likely to have diabetes than others. For example, while an estimated 13% of adults in the U.S. have diabetes [3], 20.5% of U.S. Veterans have diabetes; the percentage increases to 25% of patients receiving health care at the Department of Veterans Affairs (VA) [4].

One of the damaging effects of increased blood sugar levels is the deterioration of capillaries. A damaged capillary system can reduce blood flow to the limb extremities, therefore degrading the surrounding tissue. A common effect of having diabetes is the deterioration of foot health. This can lead to issues including peripheral neuropathy and the stiffening of the plantar soft tissue [5, 6]. Peripheral neuropathy is the loss of sensation at limb extremities due to nerve damage. This is troubling because without feedback from the environment, the foot could sustain stress and injury

without the person's awareness until inspected. With stiff plantar soft tissue, repeated stress and strain on the foot can lead to foot ulcerations, which is the breakdown of plantar soft tissue [5, 6]. Ulcerations can start under the skin and work their way toward the skin surface, eventually exposing the foot tissue and bones [7, 8]. The locations of the foot that are at high risk for ulcerations include the heel pad and forefoot [9]. Even when ulcerations heal, the tissue is still at risk for re-ulcerations. Those who have had ulcers are at an increased risk for another ulcer compared to those who have never had them [7, 10]. If conditions worsen, for example through infection, amputation may be required [5, 6, 7, 8, 9]. Those who have had ulcers are at an increased risk of death [11].

1.2 FOOTWEAR SOLUTIONS FOR DIABETES-RELATED FOOT COMPLICATIONS

Patients with diabetes may be prescribed therapeutic footwear to help reduce pressure in high-risk ulceration areas of the foot [12, 13]. A total contact cast is regarded as the best solution for ulcer healing and prevention, although it severely limits foot mobility which can make daily life challenging [12]. Outside of therapeutic footwear and total contact casts, some have explored ways to customize footwear to improve the lives of those with diabetes. For example, one group has designed novel footwear that helps regulate foot temperature because temperature can affect foot ulceration risk, although the footwear's effectiveness in reducing this risk has yet to be determined [14]. Along with footwear, orthoses may be prescribed to help alleviate stress at high risk areas for ulcerations. It is possible to design and manufacture custom orthotics to help reduce plantar stress and strain [8, 15, 16]; this is made easier with the use of additive manufacturing [16, 17, 18].

1.3 METHODOLOGIES IN CAPTURING FOOT DATA

In order to continue improving on solutions for diabetes-related foot complications, greater understanding of diabetic foot biomechanics is a must. It can be a challenge to determine if the patients have stiff plantar soft tissue quantitatively. Methods that capture in vivo data of the foot soft tissue during gait involved the use of ionizing radiation [19, 20]. The use of ultrasonography is a safe alternative to using X-rays, but some in vivo studies involving ultrasound have featured static conditions imposed on the feet [21, 22, 23, 24, 25, 26]. There was also a study in which ultrasound was placed flush with the floor and the test subject was able to step on the ultrasound, but the data obtained were not from true ambulation [27].

1.4 MAIN MEDICAL IMAGING MODALITIES

The four main medical imaging modalities are: X-ray/fluoroscopy, magnetic resonance imaging (MRI), computed tomography (CT), and ultrasound. X-rays work by emitting ionizing radiation to tissues. The image obtained is based on how much of the X-ray beams are absorbed by the tissue. Images are formed quickly. X-ray imaging is best used to examine bones and markers [28]. Biplane fluoroscopy uses dual X-ray systems to track bone motion. However, due to the ionizing radiation, exposure to X-rays must be limited. CT scans use multiple X-ray beams and detectors at different angles to create a 3D map of the area of interest. The use of multiple beams means that it takes some time to create the tomographic images. CT scans are good for examining bones, soft tissues, and fat. As CT scans use X-rays, there are concerns with radiation exposure. MRI works by having tissue placed in a specialized magnetic field. Detailed images are created by utilizing the polarities of hydrogen molecules within the body. The ability to image all tissues in detail comes at the cost of taking the most time of all the main imaging modalities to create the images.

As long as the patient does not have any metal plates in their body, MRI is a safe method for medical imaging [29]. Ultrasound works by sending out high speed sound waves through a medium. Diagnostic ultrasound effectively forms images in real time based on the echo received. Since the soundwaves are sent in a non-disruptive manner, there are no safety concerns with diagnostic ultrasound [30, 25]. Diagnostic ultrasound should not be confused with therapeutic ultrasound, which is not an imaging technique. Therapeutic ultrasound is the intense focusing of soundwaves at a target location that can cause tissues to heat up.

Biplane fluoroscopy and diagnostic ultrasound are the two ideal imaging modalities to study diabetic feet in vivo, especially when movement is involved. While the other two modalities, CT and MRI, have their place in studying diabetic feet [31], they generally only work with stationary bodies. So, while CT scans and MRI can provide quality imaging, they do not work when the body is moving. Biplane fluoroscopy is a unique imaging technique that utilizes a pair of X-ray image generators to create a set of images that infer three-dimensional features of the image being obtained. The VA Puget Sound has a biplane laboratory that is designed for tracking foot bone motion [28, 32].

1.5 GOAL OF THESIS

In a study done by Telfer et al., data collection of plantar foot properties with an ultrasound-embedded footwear was determined feasible (Figure 1) [33]. To build upon Telfer et al.'s work, this thesis will explain the design behind a custom image-capturing footwear for the purposes of collecting plantar soft tissue force/deformation data during gait. Data will be collected at heel and forefoot, areas that are at high risk for ulceration [9]. The sensors of the footwear will undergo a

series of validation tests to confirm their effectiveness in capturing data for future studies. The instrumented footwear will be used in a pilot study to evaluate their performance. Ultimately, the instrumented footwear will be used to study the biomechanical differences of plantar soft tissue between people with and without diabetes while ambulating. As the instrumented shoe will use ultrasound, the shoe is nicknamed "Ultrashoe." The terms "instrumented shoe/footwear" and "Ultrashoe" may be used interchangeably.

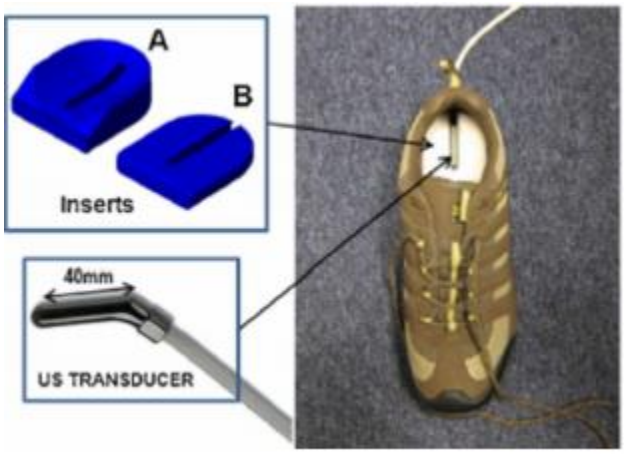

Figure 1. Set up of shoe for Telfer et al.'s study with the ultrasound probe positioned under the heel [33].

Chapter 2. INSTRUMENTED FOOTWEAR DESIGN

2.1 DOCUMENTED DESIGN PROCESS

The process of designing the footwear started with selecting a commercial sandal that fit the needs of the study. The sandal had to feature an effective foot lockdown mechanism, while also being easy to don and doff. Modeling the footwear after a sandal that featured too much upper material may make the footwear heavy, although it would feature good lockdown. On the opposite end of the spectrum, modeling the footwear after flip-flops would offer minimal lockdown, though the shoe would be easier to wear. The selected sandal model, the Skechers Outdoor Adjustable Fisherman Sandal (Figure 2), featured enough fabric straps to lockdown the foot without being too bulky. The reduced upper material would aid in the ease of access for sensors placed in the shoe.

Figure 2. The Skechers Outdoor Adjustable Fisherman Sandals selected to model the instrumented shoe after.

After purchasing the sandal model in men's size 10, it was 3D scanned using the NextEngine HD Scanner (NextEngine Inc., Santa Monica, CA). The .stl file created from the scan was imported

into SolidWorks (Dassault Systémes; Vélizy-Villacoublay, France), where it served as a model to be traced over. After recreating a computer-aided design (CAD) similar to the original scan, modifications were made to achieve desired features. These main features were to introduce two cutouts at the heel and forefoot to contain transducers (i.e., the ultrasound probe and load cells), increase the thickness of the sole to ensure enough room for the transducers, and slots in the shoe to allow straps to be sewn and lockdown the foot.

A few initial designs were made as prototypes to determine which features of the shoe were good and bad. In these early designs, the ultrasound probe to be used in the shoe had yet to be disassembled. As such, the cutout design was arbitrary and needed to be redesigned later once the ultrasound probe was obtained. The idea of having an on-the-fly adjustment of the sensors was explored. The goal was to adjust the position of the sensors laterally without removing the foot from the shoe. However, it was decided that this method of sensor adjustment would introduce greater complexity to the shoe and that it was best to keep it simple.

Initially, the slots for the fabric straps were placed in protruding tabs (Figure 3A). Although this made sewing the straps easier, there were concerns of the tabs' strength and durability. The tabs were removed, and the slots went through the shoe midsole diagonally (Figure 3B). In later designs, the diagonal slot was scrapped in favor of vertical slots that go from the top surface of the shoe to its outsole. A vertical slot made the shoe easier to 3D print and gave the fabric straps more purchase, improving shoe durability (Figure 3C). The straps of the shoe were sewn by both hand and machine. Although the original sandal model featured plastic buckle as the method of securing the foot, Velcro was used in place of the buckle to provide a custom fit and improve comfort.

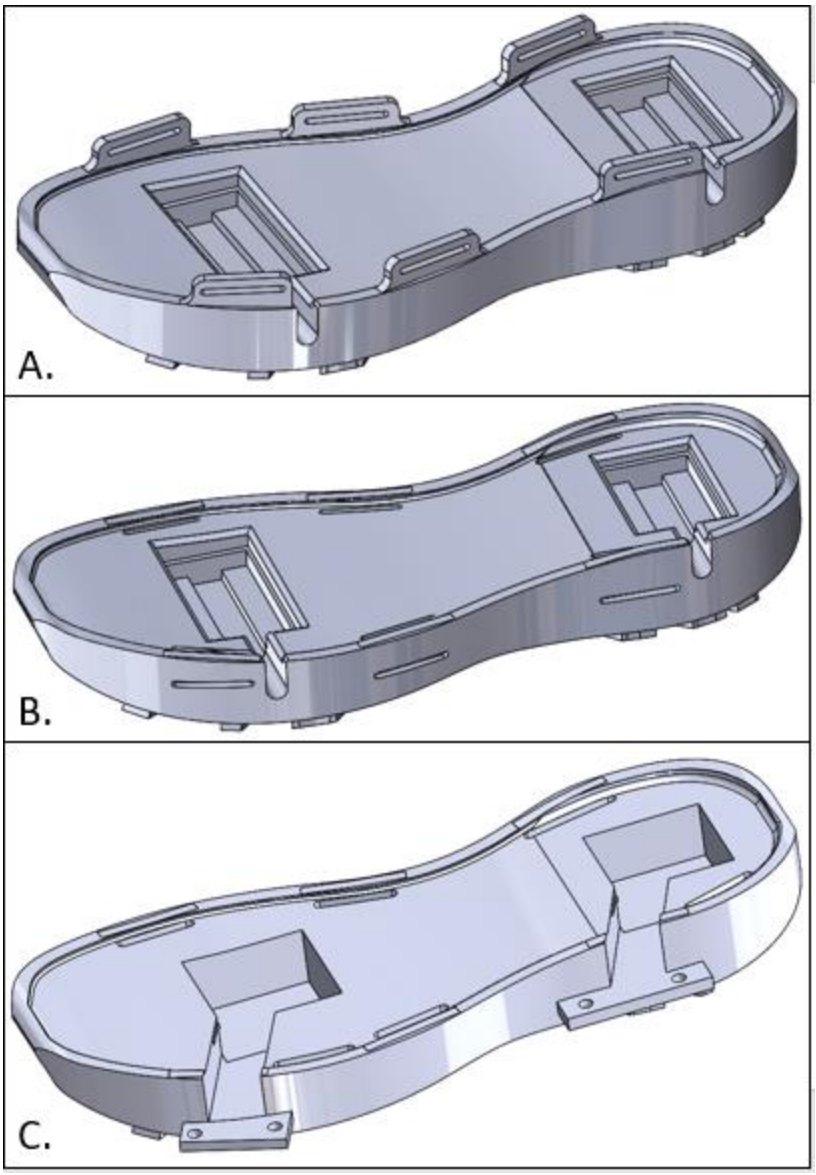

Figure 3. Early CAD models of the instrumented footwear. A) One of the first shoe designs. B) The next design iteration with altered, diagonal slots for the straps. C) A later design that better accommodates the sensors and where the strap slots go straight down.

Receiving the disassembled ultrasound sensor helped guide future design iterations of the shoe. The ultrasound cable was oblique to the ultrasound probe (Figure 4). To avoid potential damage to the cable, it was decided that instrumented shoes would only be worn on the left foot. In the shoe, the ultrasound cable came out laterally, angled anteriorly. The sensor cables exiting laterally

helped prevent test subjects from potentially tripping and causing harm to themselves or damage to the equipment. The lateral cable channel featured some rigid lip extrusions near the top surface of the shoe. These lip extrusions were designed to help keep a custom cable cover piece in place. The bottom surface of the channel cutout was extended slightly to provide further support for the ultrasound cable. Both the lateral extended surface of the cutout and the cover piece featured two holes. These were intended to allow optional screws to come through and help clamp the cable covers in place, providing strain relief to the cable (Figure 5).

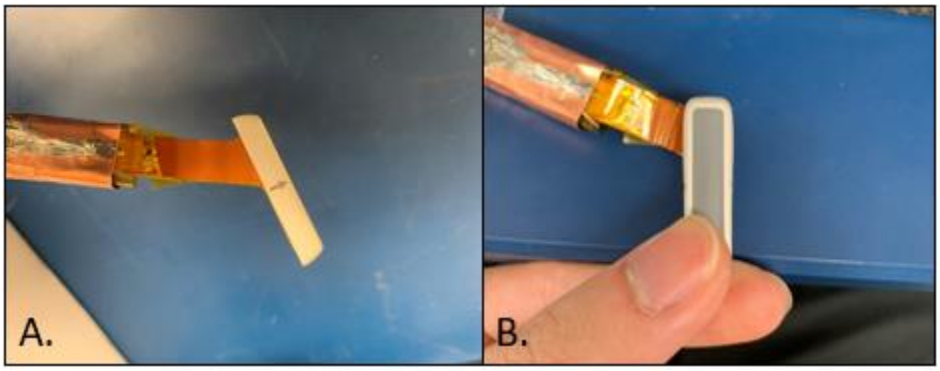

Figure 4. Images of the disassembled ultrasound probe. A) Unbent probe. B) Bent probe.

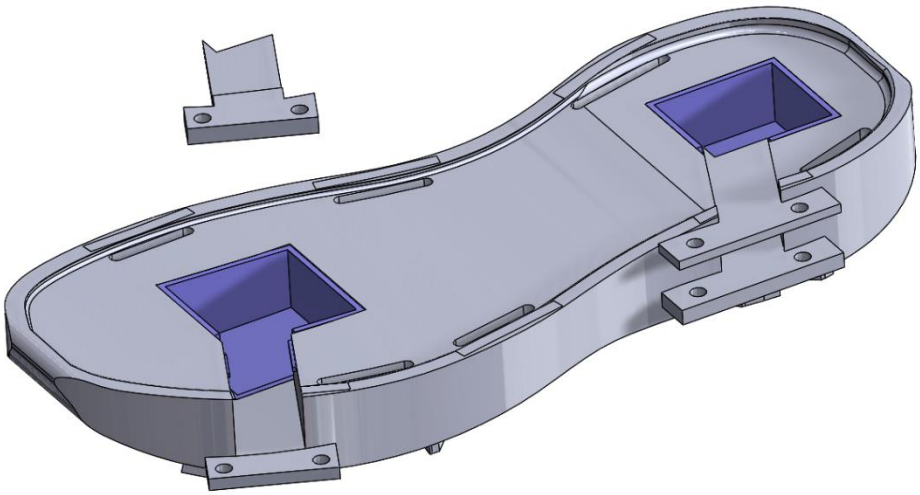

Figure 5. Updated shoe CAD. Blue surfaces indicate rigid regions. Cable cover piece can be seen above the shoe's forefoot region.

The cutout design for the sensors was refined to allow all the sensors to fit within the shoe and to adjust its position in the mediolateral direction. Sensors were held in place by a custom cover that also protected the sensors from the foot. In the initial design, the surface of the cutouts was made rigid (Figure 5). The idea behind this was to provide the load cells a hard surface to sit on in order to output accurate force data.

The first shoe prototype was 3D printed in-house with the Connex3 Objet 350 (Stratasys; Eden Prairie, Minnesota). The Objet 350 uses PolyJet Technology to print the material. Compared to most commercial 3D printers, which use the fused deposition modeling (FDM) technology, the PolyJet technology creates accurate print jobs within 0.1 mm that can feature several material properties in one print [34]. One drawback of using PolyJet technology is the higher cost of resin compared to thermoplastic filament used by FDM.

In this thesis, the shoe was printed with the Tango resin and the Digital ABS Plus resin. Specifically, the shoe was mostly comprised of the Tango resin (FLX95585-DM), a mixture of the Tango Black Plus resin and the Digital ABS Plus Ivory resin. The Tango material's hardness was made to be Shore A 85 to create a durable, yet pliable material. Its pliability gave the shoe flexibility, comfort, and traction. The Digital ABS Plus resin (RGD5131-DM), a mixture of Stratasys' resins RGD515 and RGD531, was the material for the rigid components of the shoe.

After 3D printing a prototype of the shoe above, it was determined that the rigid surface of the sensor cutouts broke upon shoe flexing (Figure 6). This was a primary concern moving forward as the shoe's durability and the ability to collect data were in question. Other concerns were the noticeable stiffness and weight of the shoe. The original commercial sandal that was purchased (Figure 2) weighed about 241 g. In comparison, the first full prototype weighed about 700 g. With so much resin used in the 3D print, the shoe was also very stiff, making it hard to flex.

Figure 6. The first instrumented shoe prototype for men's size 10 3D printed with the Stratasys Objet 350. Straps and Velcro were sewn on. The entire shoe weighed about 700 g.

To address the issue of shoe durability, the rigid casing of the cutouts was removed. Transitioning material hardness from pliable to rigid was one of the factors that caused the shoe to break during flexing. The hard surfaces of the cutouts were removed and made to simply be the same material as the bulk of the shoe. Fillets were added in and around the cutouts to minimize stress risers. The next thing done to improve shoe durability was readjusting the forefoot cutout position. The forefoot cutout was moved slightly more posteriorly to better capture the second and third metatarsal heads while avoiding the greatest flexing point of the shoe. The location of the metatarsal heads was guided by an anthropometry technical report [35]. In addition, the bottom side of the cutouts were extruded to be flush with the sandal treads. This gave the cutout more material to withstand the force imparted to it by the sensors during ambulation.

To address the shoe stiffness, two flex zones were added adjacent to the forefoot cutout anteriorly and posteriorly. The flex zones were regions of the shoe that feature a softer material than the rest of the shoe. It was possible to achieve a softer material by adjusting the resin mixture; the hardness was reduced to Shore A 45 which made the material more compliant. The flex zone regions were designed as a “V” strip that runs across the shoe laterally (Figure 7). Not only was this design intended to improve the shoe flexing, but it was designed to also help dissipate the flexing stress at the forefoot cutout, theoretically improving the shoe durability.

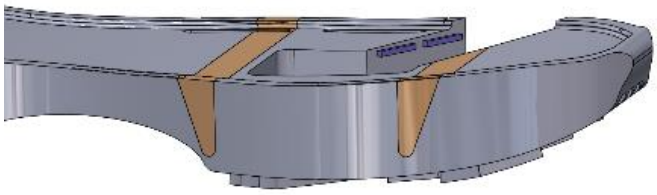

Figure 7. A shoe CAD featuring the flex zones shown in orange.

To reduce weight, two actions were taken. First, the arch of the shoe was made thinner; this had the added benefit of improving shoe flexibility. Second, a grid design was placed on the sole of the shoe and cut extrusions were made to reduce mass (Figure 8). Applying these changes resulted in a new mass of approximately 550 g, albeit for a men's size 9 shoe.

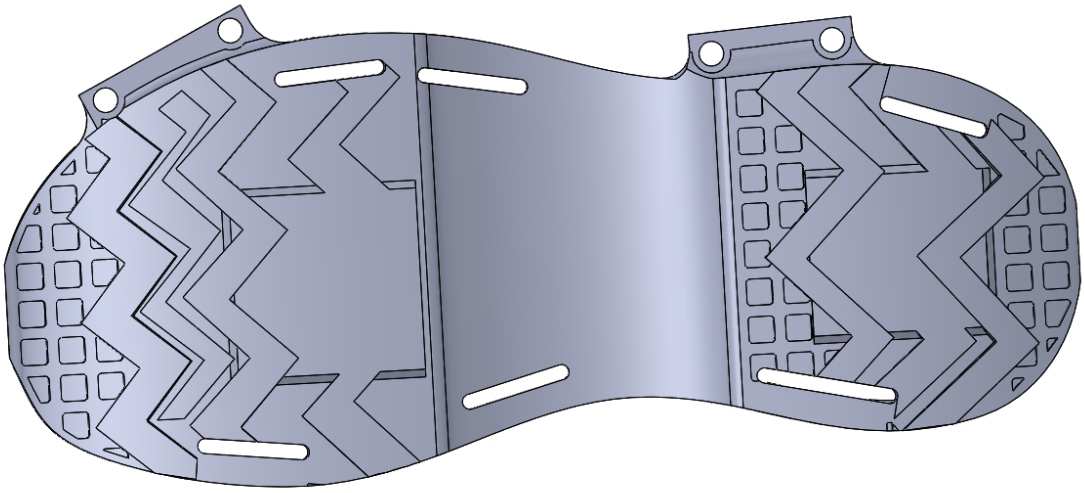

Figure 8. Bottom view of the shoe. The traction pattern and grid cutouts can be seen.

After further inspection and informal testing of an updated prototype, the shoes were ready to be 3D printed for use (Figure 9). The shoes were printed in men's sizes 5, 7, 9, and 11, where men's

sizes 5 and 7 could be treated as women's sizes 7 and 9, respectively. Size scaling was inferred by the anthropometric report [35].

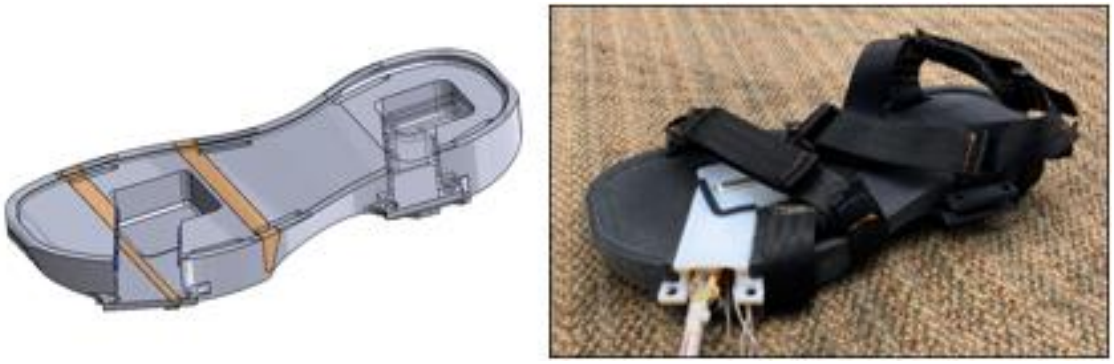

Figure 9. CAD of final shoe (left) and a picture of the 3D printed shoe (right).

An insole cover was placed on top of the instrumented shoe for added comfort. The insole was a simple thin foam material with cloth covering one side. The insole material was cut to fit the shoe and accommodate for the sensors. A gel pad was be used as the medium between the ultrasound sensor and the plantar surface of the foot.

The probe clamps (Figure 5) were designed to keep the ultrasound probe in place and provide some strain relief for the probe cables. In the final design, the probe clamps merged with the probe covers; the components are now called the "case cover".

2.2 OTHER COMPONENTS OF THE INSTRUMENTED FOOTWEAR

The instrumented shoe was accompanied by various components that help facilitate the shoe's effectiveness for capturing data. Throughout the design process there were additional components created that were tested and rejected, either because they were deemed unnecessary or have been assimilated into another design, e.g., the cable covers (Figure 5) that became a part of the case

covers. The removed components will not be explored in this thesis. All of the components described below were 3D printed by the Stratasys Objet 350. They were all rigid components unless otherwise stated.

The first component was the load cell plate (Figure 10). It was a small bracket designed to hold four miniature load cells. There were two load cell plates; one was flat and designed for the heel, while the other was angled slightly by about 1.89° and was designed for the forefoot (Figure 11). The reasoning for the angle was to get the line of action of the sensors close to perpendicular with the curve of the shoe's forefoot surface. The load cell plate sits at the bottom of the cutout.

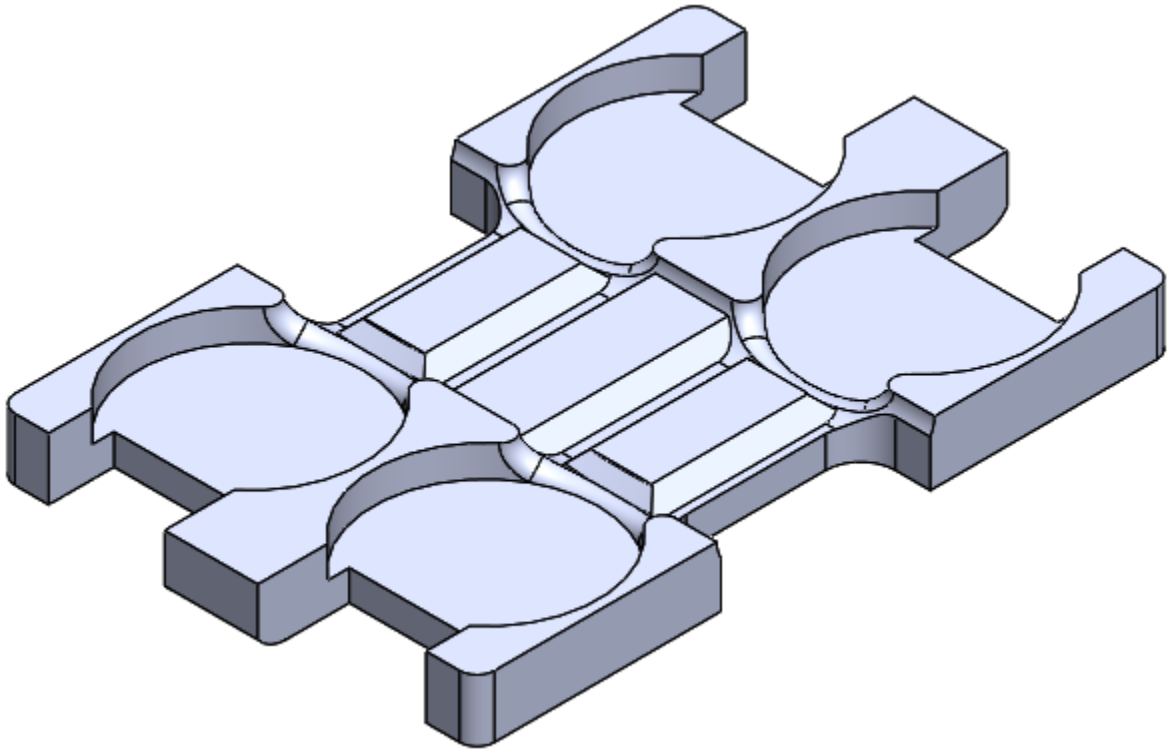

Figure 10. The load cell plate in isometric view.

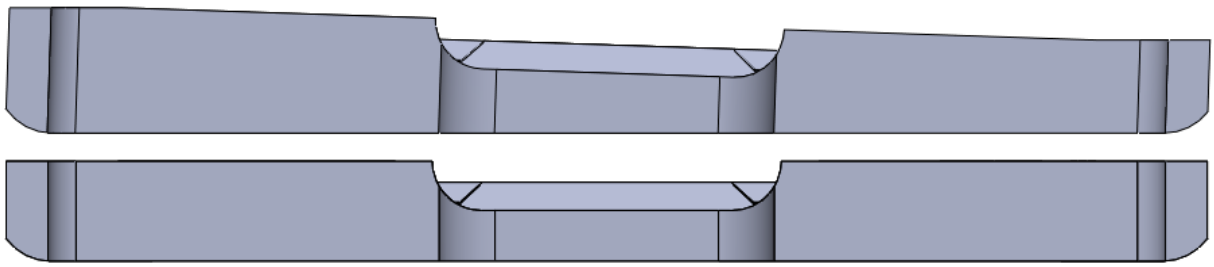

Figure 11. Lateral view of the load cell plates, where the heel variation is on the bottom. Notice the angle introduced in the forefoot variation, shown in the top load cell plate.

The next component was the probe case (Figure 12 and Figure 13). It was a two-piece unit that encased the disassembled ultrasound probe. It was designed to sit on top of the four load cells and transfer any force imparted on the probe to the load cells.

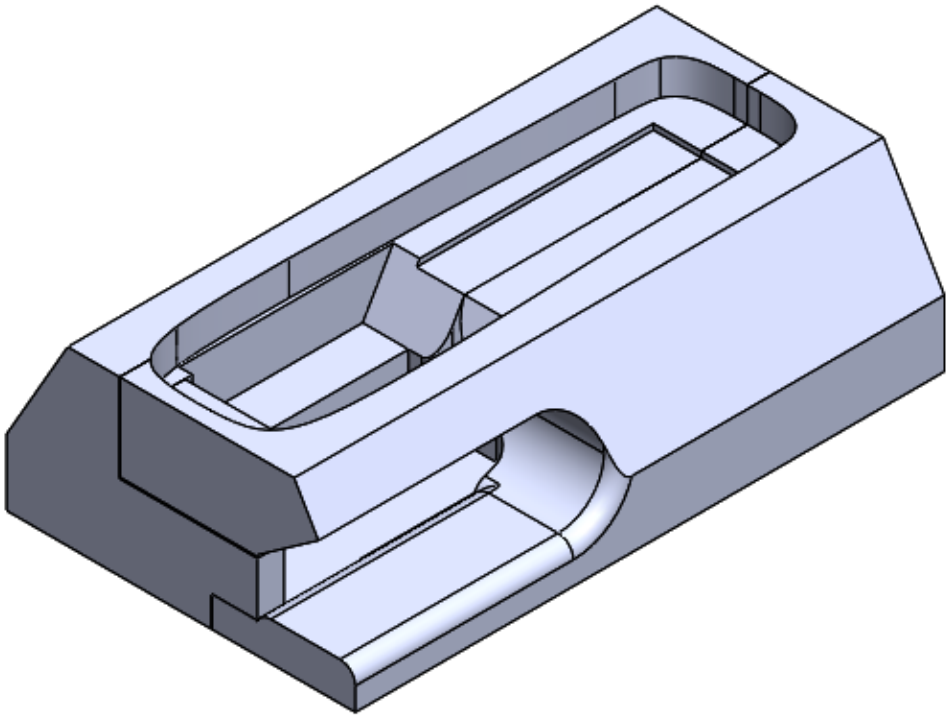

Figure 12. The probe case in isometric view. It is made of two parts.

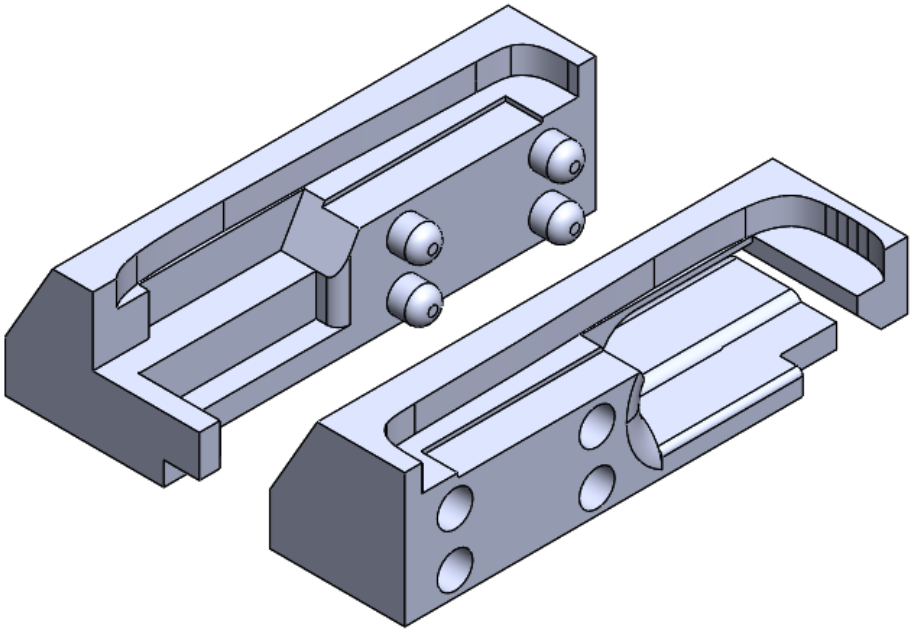

Figure 13. The probe case disassembled, showcasing how the pieces snap together. The piece on the right has been rotated 180 degrees.

The case cover held the load cell plate, load cells, probe case, and ultrasound probe in place once they were inside the shoe's cutout (Figure 14). The case cover also extended out laterally to cover and protect the sensors' cables. The cover's extension was joined to the cover's main body by a region of stiff, but still compliant, material of Shore A 85 hardness. The high hardness value ensured the cover remained sturdy while allowing some dissipation of stress caused from shoe flexing. The heel and forefoot cutouts had their own case cover; while the top surface of the heel's case cover remains flat, the forefoot's case cover had a slight curve to be flush with the shoe's forefoot surface. In addition, other case covers were designed with the ultrasound probe opening at different medial or lateral positions. This was to accommodate for the different positions the sensors could be located. The case cover's opening position was different for the heel and forefoot. For the heel, possible positions were ± 2 mm and ± 3 mm medial/lateral. For the forefoot, possible positions were ± 2 mm, ± 4 mm, and ± 6 mm medial/lateral. This provided 10 different variations

of the base case covers from the neutral position, and in total there were 12 case covers to choose from (five different positions at the heel and seven different positions at the forefoot). This flexibility allowed for the positioning of the ultrasound probe beneath the heel or either the second or third metatarsal head.

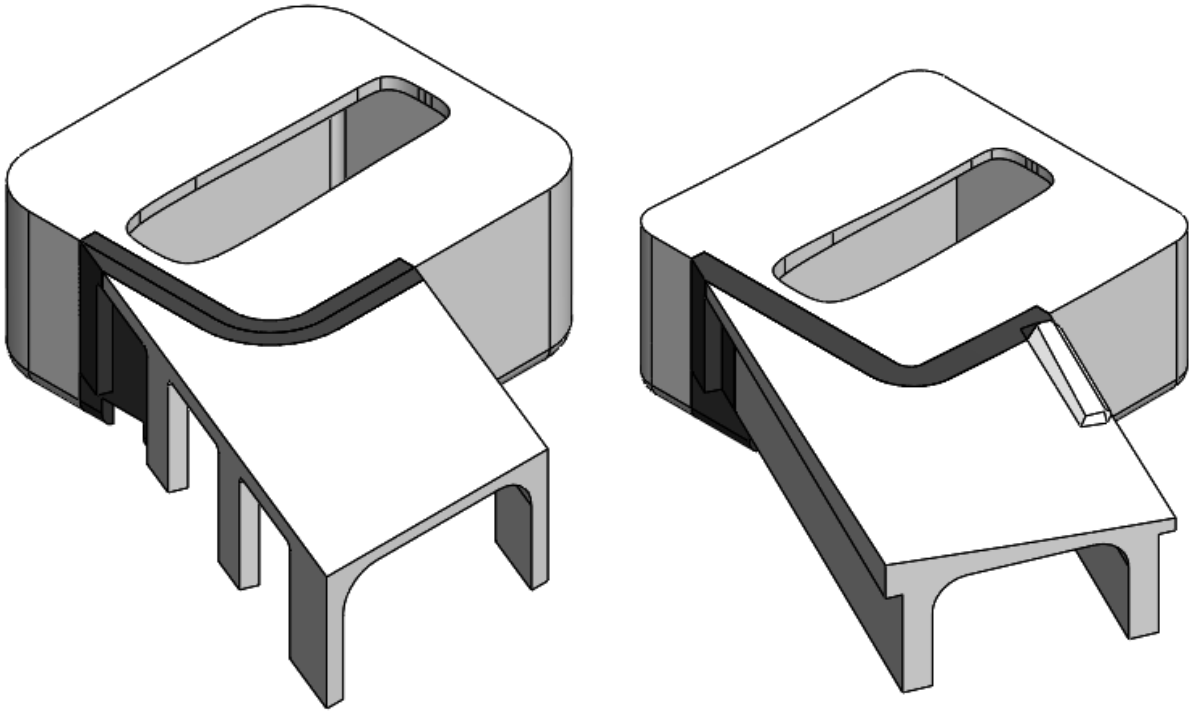

Figure 14. The case covers in isometric view. The heel variation (left) has a flat top surface, whereas the forefoot variation (right) has a curved top surface to fit flush within in the instrumented shoe.

The filler piece was a stiff homogeneous material 3D printed with a hardness of Shore A 85 (Figure 15). It filled in the entirety of a shoe's cutout (sensors and cables) when it was not in use. This allowed the test subject to walk in the instrumented shoe when one or both of the cutouts was not instrumented. The heel and forefoot had their own filler piece designed for their unique cutout

shape. The forefoot filler piece was made of both the stiff material and the softer material of hardness Shore A 45 to accommodate for the forefoot flexing.

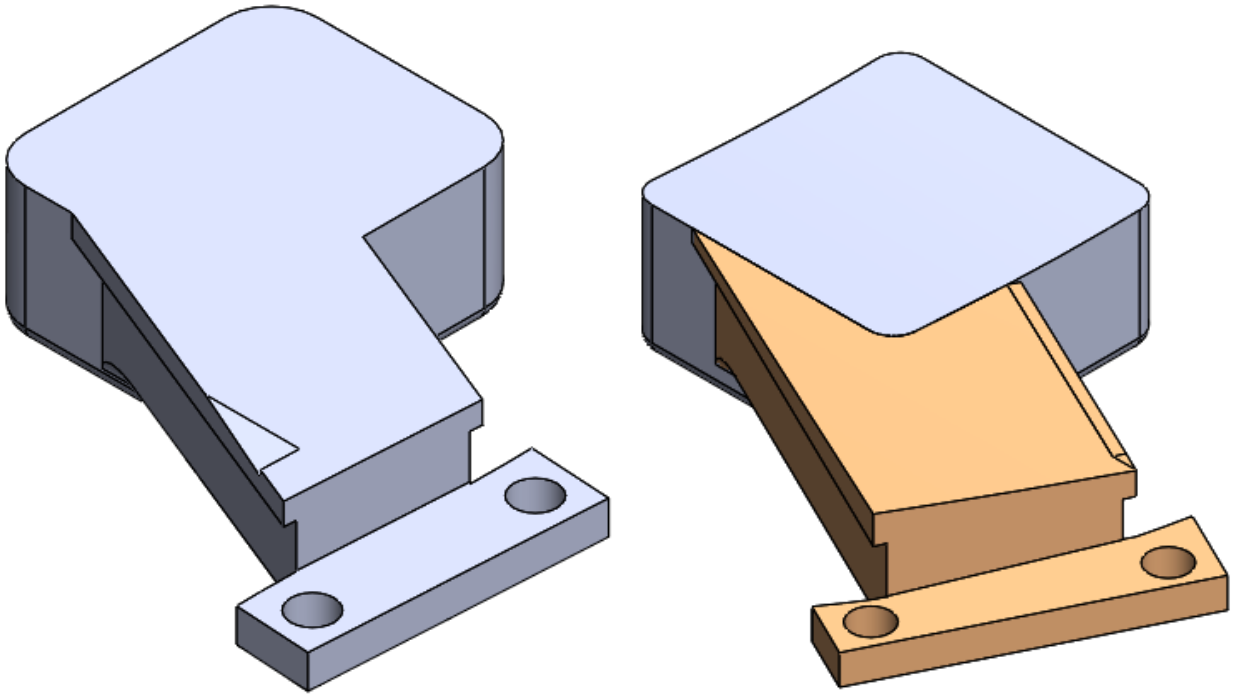

Figure 15. The filler pieces in isometric view. The material of the heel variation (left) is homogenously made of a firm, but still pliable, material. The forefoot variation (right) features a softer region, depicted in a light orange shade where the sensor cables would be.

The placement tool was an assistive tool designed to help place the case covers over the sensors in shoe (Figure 16). It was a rigid column piece that is intended to insert through the opening of the case cover prior to covering the sensors in shoe. Once through, the column was placed on top of the ultrasound probe and held firmly to help keep the sensors in place. Once the sensors were positioned properly, the case cover could be lowered down in the cutout to cover the sensors.

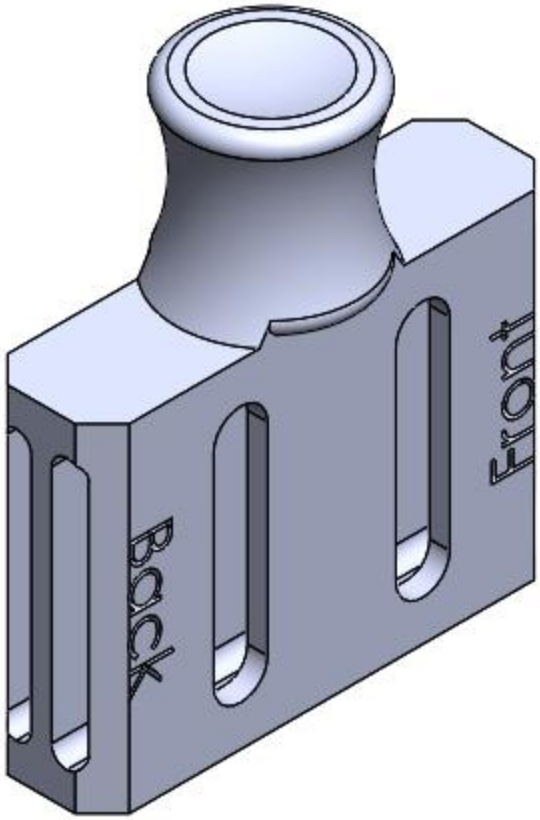

Figure 16. The placement tool in isometric view. Its use is optional but can help with placing the case covers over the other components that reside within the instrumented shoe cutout.

Chapter 3. SENSORS

3.1 ULTRASOUND SYSTEM

Of all the main medical imaging modalities (X-ray, MRI, CT, ultrasound), an ultrasound system was selected for several reasons. Ultrasound provides real-time imaging and does not present any dangerous ionization risk for the test subjects, as is the case with X-ray and CT imaging. Ultrasound is also an ideal modality for imaging soft tissue. Finally, using MRI or CT scans would yield higher quality images, but dynamic imaging is not possible.

The Aixplorer ultrasound system (Figure 17) by SuperSonic Imagine (SSI) (Aix-en-Provence, France) was used for this study. The ultrasound probe selected was the SLH20-6 (Figure 18), nicknamed the “hockey stick” due to its shape. The SLH20-6 had 192 elements and its bandwidth, or the range of ultrasound frequency, ranged from 6 to 20 Hz. This probe was selected out of others due to its small footprint.

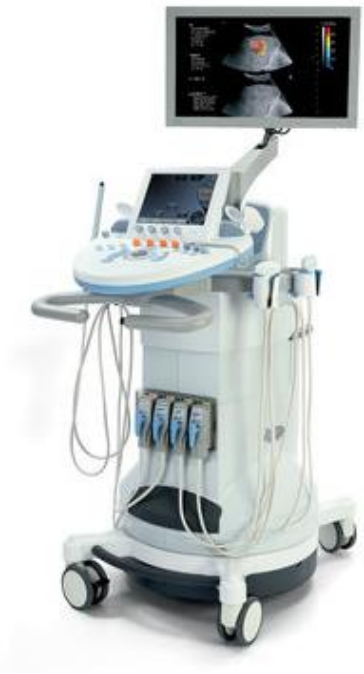

Figure 17. The Aixplorer ultrasound machine by SSI. Image taken from the SSI website.

Figure 18. The SLH20-6 ultrasound probe. Image taken from the SSI website.

In its original form, the probe could not be fit in the shoe. For this study, it was required that the probe's casing be removed. There was a risk of damaging the probe if removing the case was attempted without the aid of the manufacturer, and any damages made to the ultrasound cable could affect the image integrity. With the help of Matt Bruce, PhD from the Applied Physics Laboratory (APL) at the University of Washington, a SLH20-6 probe was disassembled (Figure

19) by Humanscan (Gyeonggi-Do, South Korea), the manufacturer of this ultrasound probe. Once the probe was disassembled, it was quite fragile and had to be handled with care.

Figure 19. A disassembled SLH20-6 ultrasound probe.

Liquid gel, commonly used as the medium between an ultrasound probe and tissue, was not used in this thesis. Test subjects will induce non-static forces on the probe that would easily displace any liquid gel. Rather, gel pads (Figure 20) from Parker Laboratories (Fairfield, NJ) were purchased to be used instead. Gel pads are a firm, gelatinous material that acts as the ultrasound medium. The gel pad is less messy and reduces the need to replace the ultrasound medium frequently.

Figure 20. Ultrasound gel pad. Image taken from the Parker Laboratories website.

The gel pad was cut by using a handheld cheese cutter (Figure 21) and trimmed with a box cutter. Using a cheese cutter resulted in a gel pad with a more uniform thickness (approximately 5 mm). A box cutter was used to cut the gel pad into a rectangular shape that fit within the insole over the ultrasound probe.

Figure 21. The cheese cutter used to cut the gel pad with relatively uniform thickness. Image taken from the Amazon website.

3.1.1 Summary of optimal ultrasound setting

Once the disassembled SLH20-6 probe was connected to the Aixplorer ultrasound machine, the settings were adjusted to achieve the best imaging quality possible. Changing the settings to achieve the highest frame rate was the main priority, as a higher frame rate would provide better ultrasound videos. Only some of the settings affected the machine's frame rate. The settings that did not affect the frame rate were still adjusted to help improve image quality. The ideal settings are listed below (Table 1). For instructions on using the Aixplorer ultrasound machine and an in-depth explanation of the settings, refer to Appendix A.

Table 1. A summary of optimal settings for the Aixplorer ultrasound machine.

Settings	Selected option	Effects on system
Harmonic imaging	Off	Affects frame rate. Selecting “on” reduces frame rate.
SuperCompound	On	Affects frame rate. Selecting “on” increases frame rate.
Res / Gen / Pen	Res	Affects frame rate. Although selecting “Pen” would increase frame rate, the SLH20-6 max frame rate is 45 Hz. Based on these settings, selecting “Pen” would not increase the system’s frame rate any further.
HD / Fr. Rate	Med	Affects frame rate. Although selecting “Fr. Rate” would increase frame rate, the SLH20-6 max frame rate is 45 Hz. Based on these settings, selecting “Fr. Rate” would not increase the system’s frame rate any further.
Zoom	Custom HD Zoom	Affects frame rate. A magnified section of the ultrasound may increase frame rate. Zoom into the region of interest where the bones are likely to appear.
Dynamic Range	50 dB	Does not affect frame rate. A dynamic range of 50 dB helps make the image appear brighter. Ultimately this setting is not crucial and is more of a preference.
SuperRes	1	Does not affect frame rate. SuperRes is a setting that can improve image textures by reducing speckles. A value of 0 would have given the best speckle images, but a value of 1 helps ensure the image quality is still acceptable. Speckled images are desired when analyzed with digital image

		correlation (DIC). DIC is a potential technique to analyze ultrasound images in the future.

3.2DATA ACQUISITION—LOAD CELLS AND LABVIEW

The load cell model selected for the instrumented footwear was the Honeywell Model 13 Subminiature Load Cells (Morris Plains, NJ). This model was selected for its small size; the load cell's diameter is 0.375 inches (9.525 mm) and it is 0.12 inches (3.048 mm) in height. Each load cell is rated for a compression load of 250 lbs (1112 N). Its cable length is approximately 20 feet (6.096 m), which provided ample length for the test subjects to walk several steps. Four load cells were placed in the custom load cell plate of the instrumented shoe. Having four load cells helped physically balance the ultrasound probe casing during ambulation. It also effectively increased the maximum total force input by dispersing force between the four load cells.

The load cells were wired into an input/output module that was connected to a data acquisition chassis (National Instruments; Austin, Texas). The data acquisition chassis model used was the cDAQ-9178 and the I/O module used was the NI-9237, a strain/bridge input module. The load cells were wired into via a D-Sub connector. Force data acquisition was facilitated by the LabVIEW (LV) analysis software.

3.2.1 Explanation of LV code

The LV code used in this thesis was custom written for collecting the four load cell data. It follows the queued message handler (QMH) design pattern, which is a variation of the producer/consumer design pattern. In the producer/consumer design pattern, the code would have two while loops—

one producer loop and one consumer loop. The producer loop is responsible for creating tasks for the code to process. The consumer loop takes in tasks from the producer loop and completes them. This is a simple yet effective design because it allows the code to process user input and tasks simultaneously. Without this design pattern, it is possible for the user to input a command to the software and wait for the software to complete its task before the user can input another command. The producer/consumer design pattern ensures that the user can always input a command as the software processes the commands in the background. In the QMH design pattern, the term "tasks" will be referred to as "messages." The QMH is named so because the user input is treated as queuing a message. The code then dequeues the message, reads the message, and takes the appropriate action. The QMH expands on the producer/consumer idea by allowing the consumer loop to produce and enqueue messages. By giving the consumer loop this capability, the code's functionality is expanded.

In this project, the custom LV code is simply called "UI Main.vi." Each loop within the code is described below to explain the thought process that went into them.

Initializing Block

The initializing block was technically not a loop but should be discussed briefly. As the name might suggest, the initializing block was the section of code where variables were initialized, graphs were reset, and the system starts up. A single flat sequence structure frame was used to encapsulate the initialization process. The other loops could not start until the processing of the flat sequence structure was complete.

Event Handling Loop

The event handling loop acted as the producer loop in this code. The producer loop was provided with the initialization of the message queue. This loop contained an event structure loop that contained possible user input commands. After initialization, the event handling loop listened for the user input and was ready to perform actions based on the user's input. Tasks were executed by sending a message into the queue from the event handling loop so that the consumer loop could read the message.

Message Handling Loop

The message handling loop acted as the consumer loop in this code. The consumer loop received messages from the producer loop through the message queue and executed tasks based on the message received. For this project, the message handling loop executed the following actions: "False", "Load", and "Stop". The "False" message was simply the default action of the message handling loop, and simply did nothing. In other words, it was essentially the system waiting in standby. The "Load" message read the pathway in the "path to load" input on the front panel and displayed a graph of the saved force data. The "Stop" message, activated when the "Stop VI" button is pressed on the front panel, stopped the running LV code. Although the user could press LV's red octagon stop button on top of the front panel, it is often good practice to make a function for the LV code that stops the system properly. Pressing the "Stop VI" button outputted a confirmation message that the program ended.

Graphing Loop

The graphing loop is responsible for outputting force data that have been loaded from the user interface. It started immediately after initialization occurred. Once the graphing loop started, it continuously read from the four load cells of the project. Aside from charting the load cells readings, the graphing loop was also responsible for zeroing the load cells, converting the load cell readings from pound force to Newtons, and saving the load cell data into a text file.

The main loops of the LV code have been explained above. The functions on the front panel will now be explained. The simple front panel of UI Main.vi featured a few light indicators, a few buttons, and some charts and graphs. The light indicators helped indicate whether a certain state was true, where light that was turned on indicated true for the label it was under; most indicators were written in the form of a question to help with comprehension of the lights. The few buttons on the front panel for this study included stopping the VI, starting data collection, stopping data collection, zeroing the individual load cells, selecting a path to read the saved load cell forces, and confirming the loading of the load cell data. There were also charts and graphs for each load cell. In LV, a chart is a live plot of the current reading from a transducer. Graphs read from a saved set of data to display. Instructions to use the LV code is available in Appendix B.

Chapter 4. PERFORMANCE EVALUATIONS

It was important to inspect different aspects of the instrumented shoe and the sensors involved with data collection. As such, several tests have been done as performance evaluations. The tests range from simple, rudimentary checks to formal validation tests.

4.1 PRACTICE ULTRASOUND IMAGES/CLIPS

Several images and clips were taken before the study to become familiarized with the image and video capturing method of the Aixplorer system. The data were exported in JPEG format (for images only), AVI format (for videos only), and DICOM format (for both images and clips). The JPEG format allowed for easy access to ultrasound images and quick, simple analysis if needed. The AVI format allowed for the viewing of an ultrasound clip. Although the clip can be played, it could not be scrolled through frame-by-frame. The DICOM format allowed the user to analyze ultrasound images in greater detail. It was especially useful for analyzing clips in a frame-by-frame method. DICOM files also have embedded information about the ultrasound system used to capture the image/clip. The software used to look at DICOM files was ImageJ, an image processing software developed by National Institutes of Health (NIH) (Bethesda, MD).

4.2 ULTRASOUND FRAME RATE CHECK

A simple frame rate check was conducted to confirm the ultrasound system output (Table 2). Video captures were conducted using the SLH 20-6 probe at different sampling rates and different capture durations. The actual number of frames were observed after exporting the ultrasound DICOM files into ImageJ.

Table 2. Aixplorer ultrasound frame rate check.

Sampling Rate [Hz]	Capture Time [s]	Expected Images	Actual Frames	Lost Frames	Number of Trials	Percent Loss
17	2	34	32	2	1	5.88 %
22	2	44	40	4	2	9.09 %
44	2	88	80	8	1	9.09 %
45	2	90	81	9	16	10.00 %
45	10	450	442	8	18	1.78 %

From this simple frame rate check, it appeared that sampling rate was not a main concern in having lost ultrasound frames. Rather, it was the capture duration that seemed to reduce the percentage of frame rate lost.

4.3 ULTRASOUND VALIDATION TEST

A simple quality assurance was conducted on the ultrasound probe. Two of the SLH20-6 probes—one stock and one disassembled—were available (Figure 22). This simple validation test confirmed that the disassembled probe works as expected. The ultrasound quality assurance phantom used was the Gammex RMI 404GS LE (Sun Nuclear Corporation, Melbourne, FL). This ultrasound phantom was borrowed from the APL. Three images were analyzed for each probe. The first image captured was to test the vertical and horizontal distance accuracy. Vertical checks were distanced at 5 mm, and horizontal checks were distanced at 10 mm. The second image captured was to test the lateral and axial resolution. Both the lateral and axial resolutions had target distances of 0.25 mm, 0.5 mm, 1.0 mm, and 2.0 mm. The smallest distinguishable distance was the resolution of the probe. The third image captured was to conduct a basic geometric test on a phantom cyst, which appeared as a circular hole. The cyst had a diameter of 4 mm, and the top-to-bottom (T-B) and the side-to-side (S-S) distances were measured. Once the image was captured, they were analyzed with ImageJ. When analyzing the images obtained from the stock probe, the

pixels/mm for images one, two, and three were 15.6, 33.4667, and 33.6, respectively. The disassembled probe images had pixels/mm for images one, two and three as 15.6, 33.6, and 33.6, respectively (Table 3). Additional information on the ultrasound validation tests is available in Appendix C.

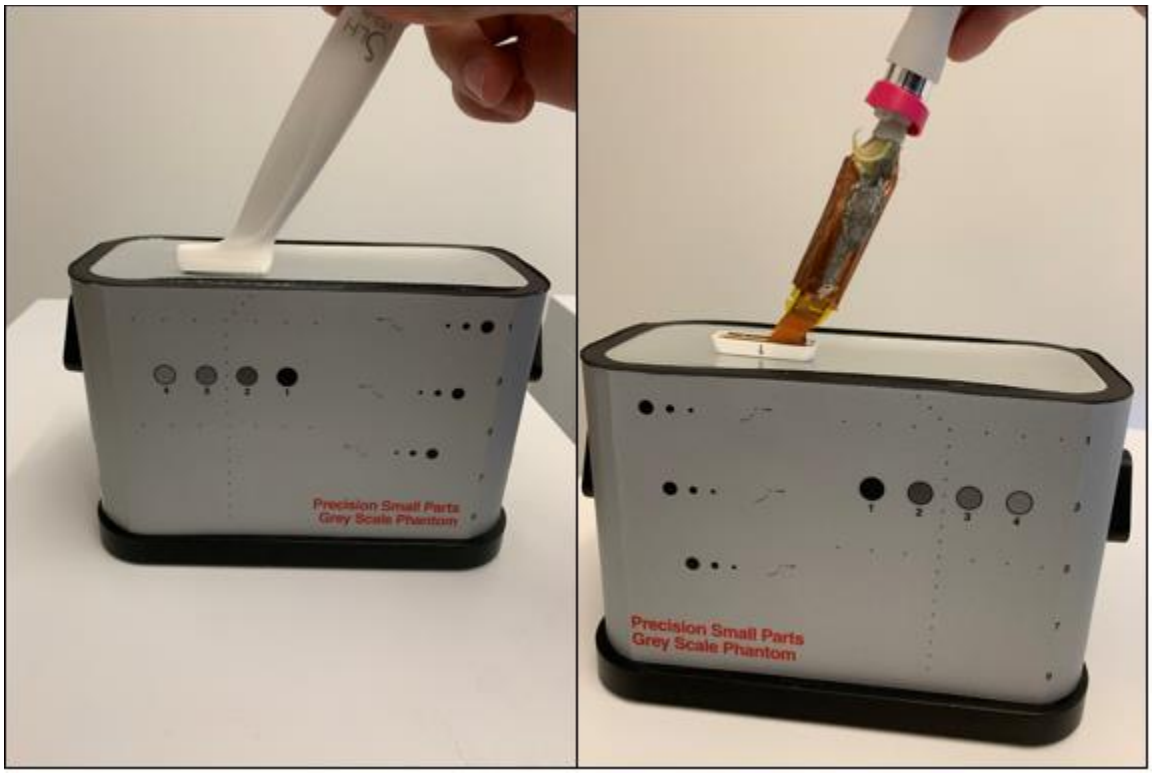

Figure 22. Ultrasound validation testing using a phantom with the stock probe (left) and the disassembled probe (right).

Table 3. Ultrasound validation test results for both the stock and disassembled (custom) probe.

Performance Test		Length [mm]		Error		Standard Deviation	
		Stock	Custom	Stock	Custom	Stock	Custom
Vertical distance		4.91	4.91	-1.8%	-1.8%	0.434	0.434
Horizontal distance		9.71	9.94	-2.9%	-0.6%	0.0460	0.363
Lateral resolution		2.0	2.0	n/a	n/a	n/a	n/a
Axial resolution		0.25	0.25	n/a	n/a	n/a	n/a
Geometric check	T-B	3.10	3.14	-22.5%	-21.5%	n/a	n/a
	S-S	3.89	3.73	-2.75%	-6.75%	n/a	n/a

4.4 CHECKING FLUOROSCOPY IMAGES WITH PHANTOM FOOT AND PROTOTYPE SHOE

The biplane fluoroscopy lab at the VA can provide high quality X-ray clips of the foot during gait. However, there were two concerns with using biplane fluoroscopy as a validation method for the data collected from the instrumented shoe. The first concern was exposing test subjects to ionization—it is always best to keep this to a minimum. The second concern was having the shoe and sensors in the X-ray shot. Having dense materials, such as the sensors, in the X-ray shot could obscure the images of the bones in the foot. If the sensors made X-ray bone tracking impossible, then exposing the test subject to ionization would have been for naught. As such, it was important to ensure that using biplane fluoroscopy would provide usable data.

A phantom foot was placed inside an older prototype of the instrumented shoe, which was 3D printed with FDM. An assembled SLH20-6 ultrasound probe was placed at either the heel or the forefoot. The X-ray machines used were a pair of modified Philips (Amsterdam, Netherlands) BV Pulsera C-arm machines. The two X-ray machines were identified by color, either as blue or green. The blue machine took X-ray images from the bottom left, whereas the green machine took images

from the bottom right (Figure 23). For testing, the foot, shoe, and sensors were placed in the target spot of the biplane. Once ready, the biplane fluoroscopy fired for a few seconds. A few trials were done to collect data that could show examples of what fluoroscopy images might look like with sensors at the heel and the forefoot (Figure 24).

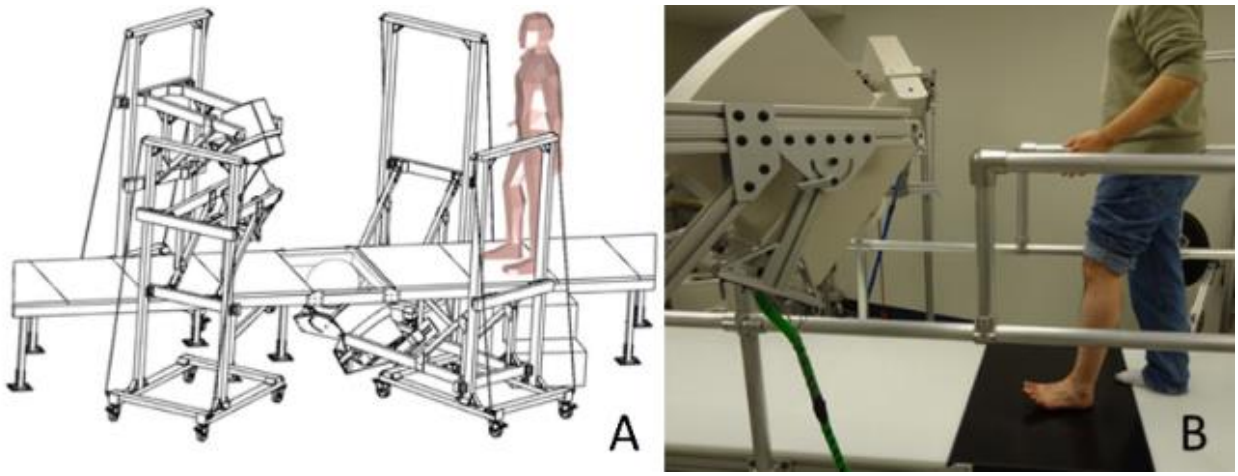

Figure 23. A) A depiction of the biplane fluoroscopy setup in the old biplane lab. B) A test subject walking through the imaging field [28].

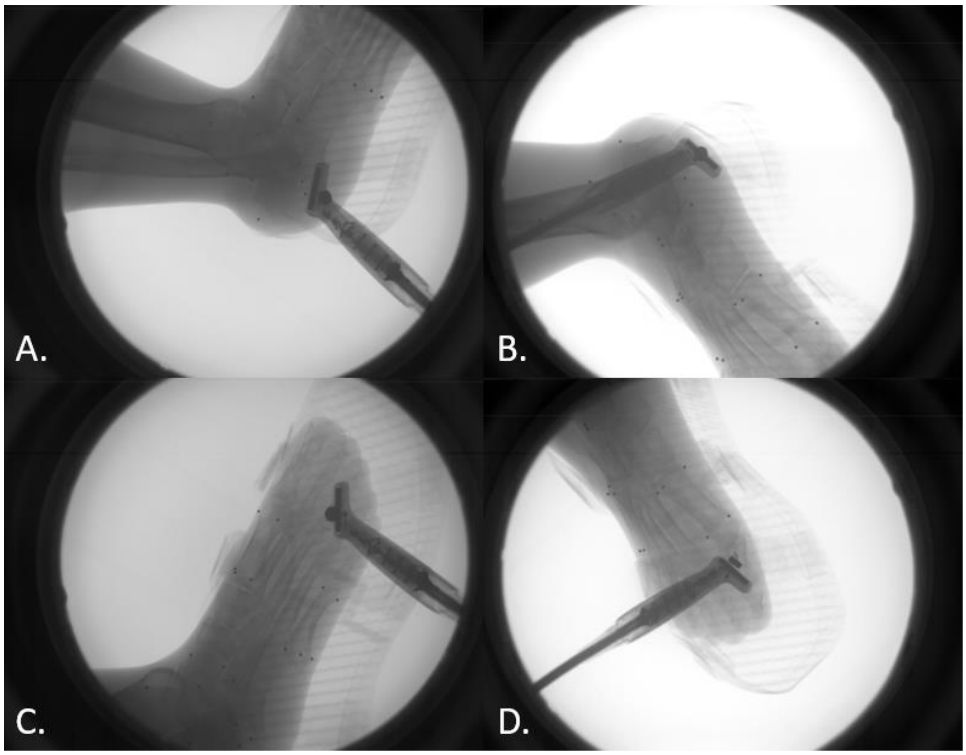

Figure 24. Biplane fluoroscopy images of the phantom foot and an ultrasound probe. The images are A) heel shot from blue, B) heel shot from green, C) forefoot shot from blue, and D) forefoot shot from green.

4.5 BIPLANE FLUOROSCOPY SIMULATION

Another fluoroscopy check was done by using a simulation feature on Mimics (Materialise, Belgium), a software for medical 3D imaging. Computer models of the shoe and its components were imported as .stl files and imposed on a CT scan of a cadaveric right foot. Since the shoe was designed for the left foot, it was mirrored prior to importing in Mimics. By combining the images of the model and the CT scan data, it was possible to simulate X-ray images. This could help infer the best set up of the biplane lab to achieve the desired images of the foot. Different angles were explored to gain a better sense of what the biplane fluoroscopic images might look like (Figure 25). The advantages to using a simulation were the freedom to explore different angles without

exposure to ionization and the ability to add in accurate models of the components for the instrumented shoe, although their imaging intensity values were estimated. Like the fluoroscopy images of the phantom foot, images of the heel (Figure 25 A, B) and forefoot (Figure 25 C, D) were captured.

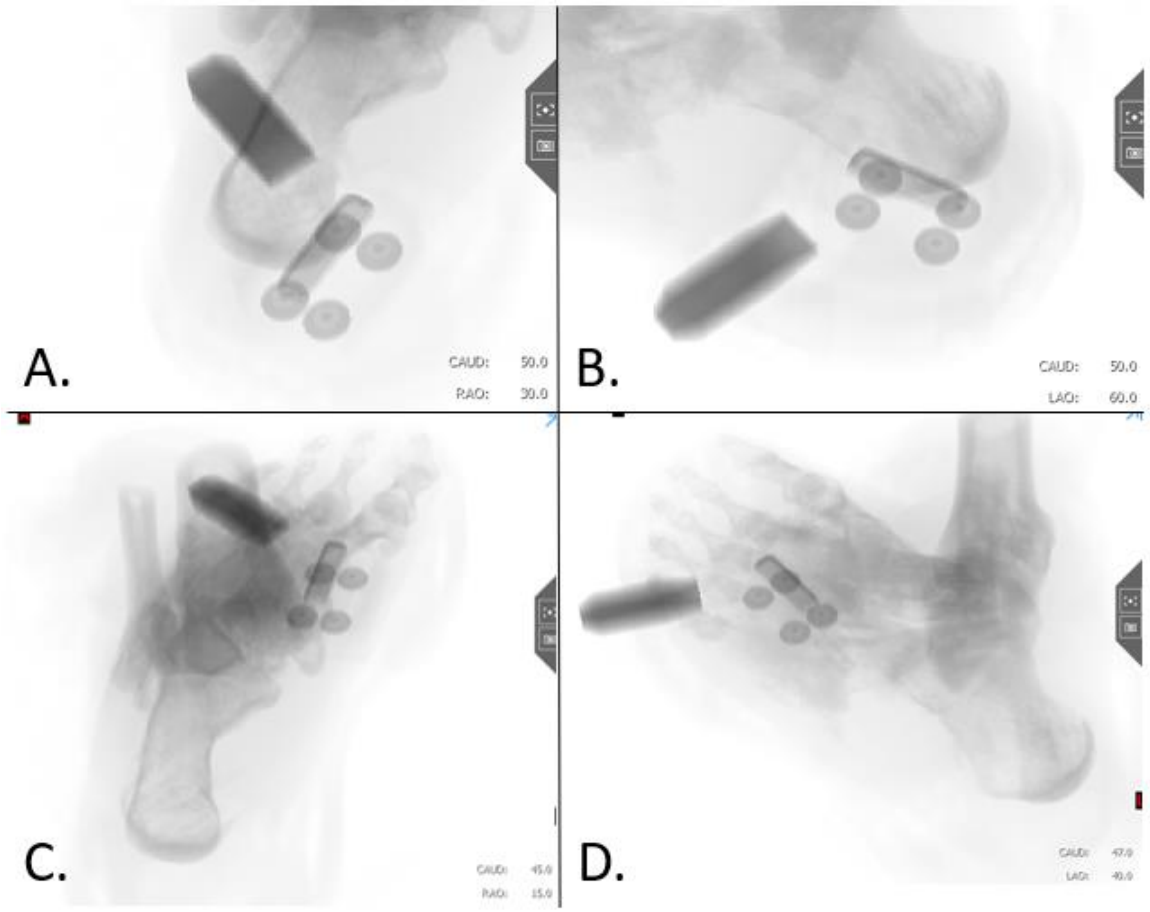

Figure 25. Screenshots of simulated biplane fluoroscopy images from Mimics featuring a cadaveric foot with CAD files of the instrumented shoes and its components. Angles featured here are: A) Caudal (CAUD): 50.0; right anterior oblique (RAO): 30.0. B) CAUD: 50.0; RAO: 60.0. C) CAUD: 45.0; RAO: 15.0. D) CAUD: 47.0; left anterior oblique (LAO): 40.0.

4.6 SIMPLIFIED TRIAL

The simplified trial test previewed what an ultrasound video and force chart might look like when placed next to another. The load cells and ultrasound system were set up to collect data in a small room. The walking distance was limited by the length of the ultrasound cable (Figure 26). Several of the simplified trials were conducted at the heel and forefoot. As this test was conducted by one person in a small room, the quality of data was affected due to altered gait. Regardless, this was the first test that collected both force data and ultrasound data simultaneously. The data were observed subjectively; there was no analysis of data in this test.

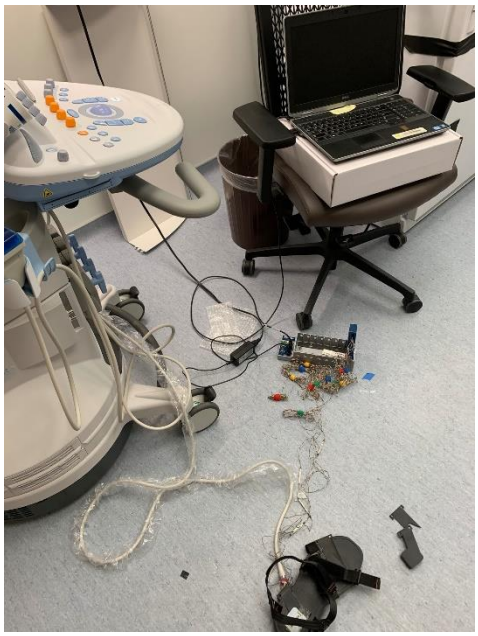

Figure 26. Setup of the simplified trials.

4.7 STATIC TESTING OF LOAD CELLS

The first formal validation test was a force static test. To confirm the proper transference of force applied on the probe sensor to the load cells, a set of static testing was performed. A set of standard

weights (22.24 N, 44.48 N, 88.96 N) were used to validate the force output of the load cells (Figure 27).

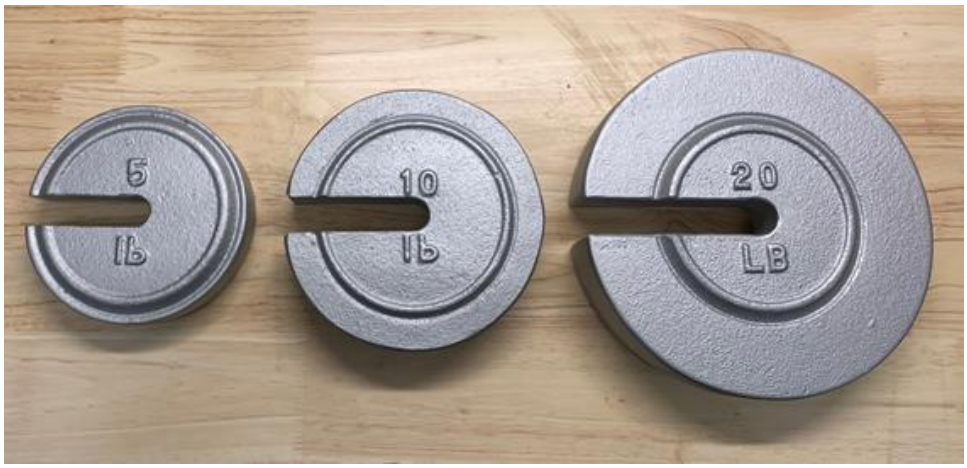

Figure 27. The three weights used for static testing, which were 5 lbs. (22.24 N), 10 lbs. (44.48 N), and 20 lbs. (88.96 N).

Ideally, the absolute error of each load cell is less than 5%. To conduct this test, the load cells were first individually tested. Each load cell was placed on a hard surface and had the different standard weights placed on them. This initial test on the individual load cells showed that each load cells were accurate (Table 4). They each had an absolute error less than five per cent. This gave confidence in moving forward with using the load cells for the other static tests.

Table 4. Average absolute error of each individual load cells after three trials.

Load cell number	22.24 N	44.48 N	88.96 N
1	1.76%	1.21%	0.84%
2	2.21%	1.02%	1.25%
3	2.44%	1.31%	2.07%
4	2.77%	2.31%	1.43%

Following the individual load cell test, they were then placed in different configurations with the shoe components; with each configuration, the load cells system increased in complexity such that it eventually resembled actual testing conditions within the shoe (Figure 28). The four testing conditions were labeled as: basic, replica, real, and shoe table top. In the basic condition, the setup was simply four load cells placed within the load cell plate. An acrylic plate was placed on top of the load cells to hold on the applied weights. The replica condition had a dummy probe placed in the ultrasound case, which was placed on top of the load cells. The acrylic plate balanced on the dummy probe. As weight was applied, it was important to keep an eye on the balance of the plate to ensure the weights did not fall over and damage any equipment. The real condition was similar to the replica condition. The only difference was that the real disassembled ultrasound probe was used in place of the dummy probe. Finally, the shoe table top condition placed the real condition inside the instrumented shoe. The shoe was placed on a rigid table top. The acrylic plate had a custom force concentrator attached to help concentrate the force directly to the probe.

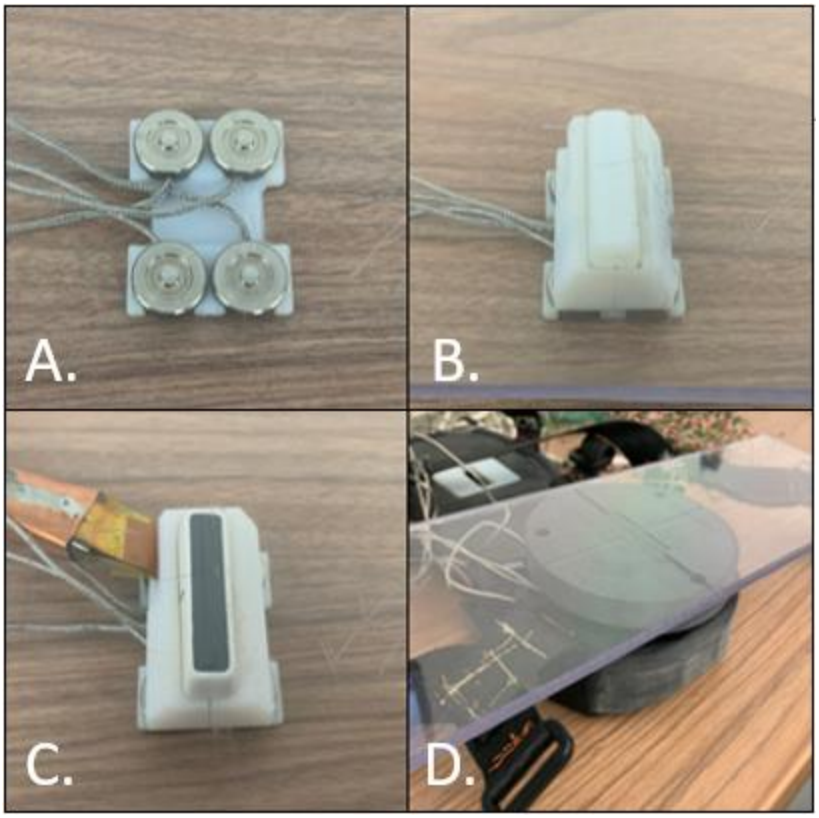

Figure 28. The different configurations for the static test. A) Basic. B) Replica. C) Real. D) Shoe Table Top.

Data collection in this test was done by placing the weights on the acrylic plate, ensuring it was physically balanced, recording the force for a few seconds, then removing the weights. The data reported were the median of the force values collected—this was done to avoid any affects unwanted noise and force spikes might have on the mean. Both heel and forefoot data were collected—what this meant was simply a change in force plates, as the heel and the forefoot cutout have their own custom force plate (Figure 11).

In the first few data collection of the static test, inaccurate data and drift was apparent in the shoe table top condition. It was determined that the ultrasound probe case needed to be redesigned, as

it did not align properly with the load cells. The static test data reported here only show the successful test. Reported are the average absolute errors of the test (Table 5); for a table of force data from each trial, refer to Appendix D.

Table 5. Average absolute error of the load cells under different test configurations.

Configuration	Location	Target 22.24 N	Target 44.48 N	Target 88.96 N
Basic	Heel	3.79%	2.70%	1.21%
	Forefoot	4.51%	2.09%	1.68%
Replica	Heel	1.39%	0.25%	1.09%
	Forefoot	1.33%	1.17%	0.39%
Real	Heel	1.85%	0.74%	1.09%
	Forefoot	0.72%	1.15%	0.72%
Shoe Table Top	Heel	1.58%	2.12%	2.35%
	Forefoot	2.44%	1.20%	1.79%

Observing the results of the static validation test, it was encouraging to see that the absolute error remained below 5%, even with increasing complexity of the test configurations. The importance of the static validation test was to gain confidence in both the load cells' accuracy and the force transfer through the rigid components.

In a separate informal test, the force was applied on the case cover, away from the probe. It was important to minimize, and ideally eliminate, the transferring of forces from the surface of a case cover to the load cells. The accuracy of analyzing soft tissue data would be reduced if the load cells picked up force outside of the ultrasound probe. In the first round of testing, the forefoot case cover transferred noticeable data to the load cell; in fact, a noticeable bend was created through one of the trials (Figure 29).

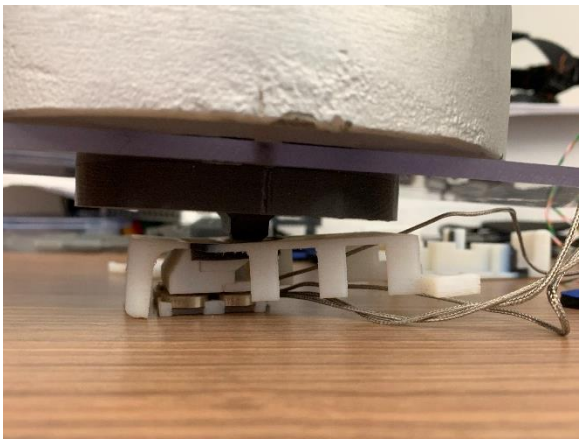

Figure 29. A static test on the side of the case covers. The force caused the case cover to bend.

This informed the design decision of introducing a wall to the anterior and posterior side of the case cover. This acted as reinforcement to resist bending on the top surface. In the next round of testing, forces applied on the case cover surface did not appear to transfer to the load cells. The updated forefoot case cover was used moving forward.

4.8 DYNAMIC TESTING OF LOAD CELLS

After the static testing was complete, the next step was to observe how the load cells respond to ambulation. To conduct this test, a thin Tekscan (Boston, MA) pressure sensor model 4201 was used. The sensor area was 21.1 mm x 45.7 mm, and its thickness was 0.178 mm. Although the sensor was rated for higher pressures (500 psi, or 3447 kPa) typical of human ambulation pressures, it could still be useful in confirming the load cell force output under dynamic conditions. The accuracy of the sensor could be improved by changing its sensitivity setting. In doing so, its saturation pressure became 647 kPa. The sensor's optimal resolution was $647 / 2^8$, or 2.53 kPa. The minimum force that will be picked up by the sensor is 2.44 N. Resolution calculations are in Appendix E. The Tekscan sensor was calibrated using an air bladder that applied uniform pressure.

Prior to conducting a dynamic validation test, a couple of preliminary static tests were done first. The first test was a simple static test on the load cells and the Tekscan sensor (Table 6). The purpose of this test was to see how the Tekscan sensor response compared to the load cells. The load cells were set up in the basic configuration from the static validation test. The Tekscan sensor was placed separately flat on a table top. The same weights (22.24 N, 44.48 N, and 88.96 N) were placed on the load cells and the Tekscan sensor. Two trials were done for each weight. The force recorded was written down from a live force output, noting the approximate consistent output. This test did not need to be formal and only served as a method to observe the performance of the Tekscan sensor.

Table 6. Static test to check the accuracy of the Tekscan 4201 sensor to the load cells under the basic configuration. The Tekscan and load cells were tested separately.

Weight applied	Load Cell (LC)	Tekscan (TS)	LC error	TS error
22.24 N	23 N	15 N	3.4%	-35%
44.48 N	47 N	39 N	5.7%	-12%
88.96 N	93 N	99 N	4.5%	11%

In this static test, the error results for the load cells were approximately 5%, but the Tekscan sensor was not as accurate, especially at lower loads. As the Tekscan sensor was rated for a higher pressure, it made sense that its greatest error occurred when smaller forces were applied.

The second preliminary test for the dynamic validation test was to observe the impact of using an insole on the load cells (Table 7). In this test, an insole was placed on top of the replica configuration from the static test (Figure 30). From here, another round of static testing began;

results shown were from an average of three trials. This needed to be explored, as an insole material will be used in shoe during the dynamic validation test and actual data collection.

Table 7. The impact of using an insole cover on the load cells.

Weight applied	No insole (off)	Insole on (on)	Off error	On error
22.24 N	22.9 N	23.0 N	3.04%	3.41%
44.48 N	46.8 N	46.2 N	5.29%	3.79%
88.96 N	93.3 N	93.3 N	4.91%	3.41%

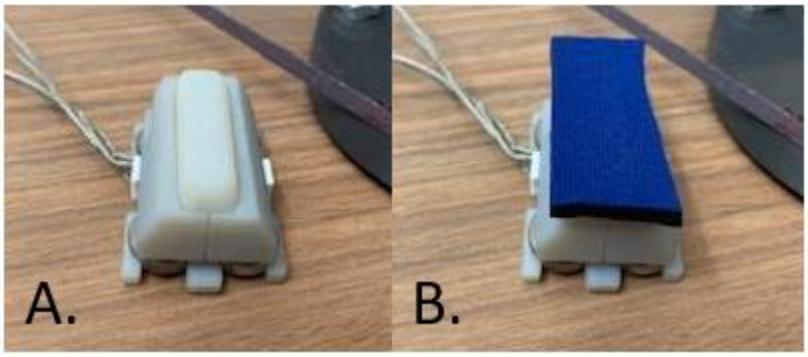

Figure 30. Test setup to explore insole effect. A) Without insole. B) With insole.

Since an insole would be used in the dynamic validation test, it was important to observe the impacts it may have on the force, especially since the insole was not a rigid component and may disperse forces in unexpected ways. Fortunately, the insole did not seem to have a negative effect on load cell accuracy during static testing.

After the second test, an additional series of tests were then conducted to determine the best way to carry out the final static testing. This involved exploring the effect of different insole shapes and the width of the force concentrator. As this information does not add much into the discussion of testing the sensors, data can be referred to in Appendix F.

The final static testing to do to prepare for the dynamic test was to introduce the Tekscan 4201 sensor in the second preliminary test (Table 8). Along with adding in the Tekscan sensor, the ultrasound case cover was introduced into the static test (Figure 31). The test results were the average of two trials. Force values were determined by noting the consistent force output of the live data.

Table 8. Static test to check the accuracy of the Tekscan 4201 sensor to the load cells under the replica probe configurations.

Test Condition	Weights	Load Cell [N]	Tekscan [N]	LC error	TS error
Table top	22.24 N	20.0	11.5	-10.1%	-48.3%
	44.48 N	41.0	35.8	-7.83%	-19.6%
	88.96 N	80.1	84.0	-9.94%	-5.58%
In shoe	22.24 N	21.4	8.88	-3.89%	-60.1%
	44.48 N	41.3	30.5	-7.27%	-31.4%
	88.96 N	80.8	84.0	-9.23%	-5.58%

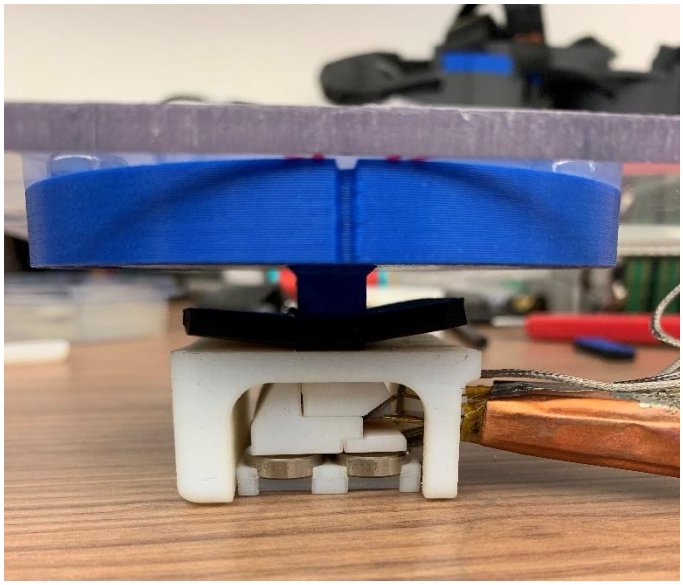

Figure 31. Testing the force readout of the load cells from introducing an insole piece and the case cover. Not pictured was the use of the Tekscan sensor.

The load cells exhibited error a little greater than expected, but it was relatively consistent across the different trials. The Tekscan sensor had high error for low force, but accuracy improved with increased weights. Through the different static tests done to prepare for the dynamic validation test, there were concerns for the accuracy of the Tekscan sensor. However, it could still be useful in informing the dynamic response of the load cells at higher loads and for timing purposes.

In the dynamic validation test, the load cells and Tekscan sensor were placed in shoe. An insole was placed on top of the instrumented shoe's surface. A person with size 9 feet wore the shoe. Once ready, the record button for both the load cells and Tekscan sensor were pressed at the same time; the record button for the load cells was on the laptop within the LV code, and the button for the Tekscan sensor was on the Tekscan handle that the sensor was connected to. Once recording started, a simple walking pattern commenced. The process was simply to start with three quick stationary taps with the left foot, wait for a brief moment, take three small steps, offload the left foot for another moment, then stand normally until the data collection finishes. The purpose of the three initial foot taps were to provide a way of synchronizing the load cell and Tekscan data. After three trials were collected at the heel, the results from each data collection medium were compared (Table 9). This test informed whether or not the dynamic response of the load cells was consistent with the Tekscan sensor response (Figure 32). The forefoot was not tested to simplify data analysis.

Table 9. Peak force recorded by the load cell and Tekscan sensor during the dynamic tests.

	Load Cell Max [N]	Tekscan Max [N]	Tekscan error to load cells
Trial 1	176.181	119.068	-32.4%
Trial 2	164.792	121.497	-26.3%
Trial 3	167.659	114.881	-31.5%

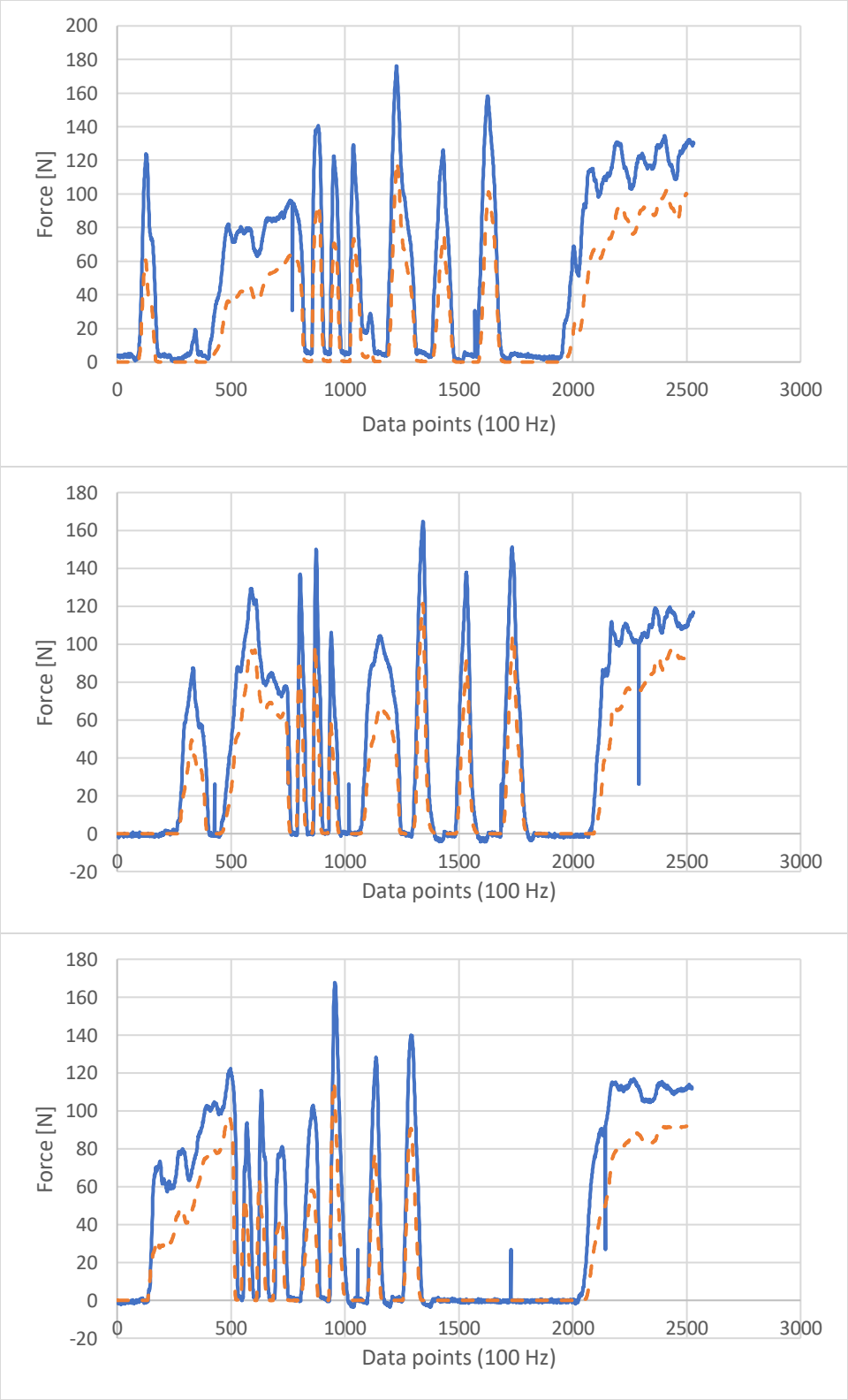

Figure 32. Load cell data (solid blue line) and Tekscan 4201 sensor data (orange dashed line) for the three trials of the dynamic test.

The force magnitude from the load cells was greater than the Tekscan sensor, which was to be expected given the static testing results. Therefore, it was difficult to conclude anything based on the magnitudes. However, the dynamic force response of the load cells was consistent with the Tekscan sensor response. To investigate this further, both the data from load cells and Tekscan sensor were normalized using the greatest peak force during the trials, then the normalized data were compared to each other (Figure 33). Verifying the dynamic force response with the Tekscan sensor helped to confirm qualitatively that the load cells did not measure any spurious peaks during gait.

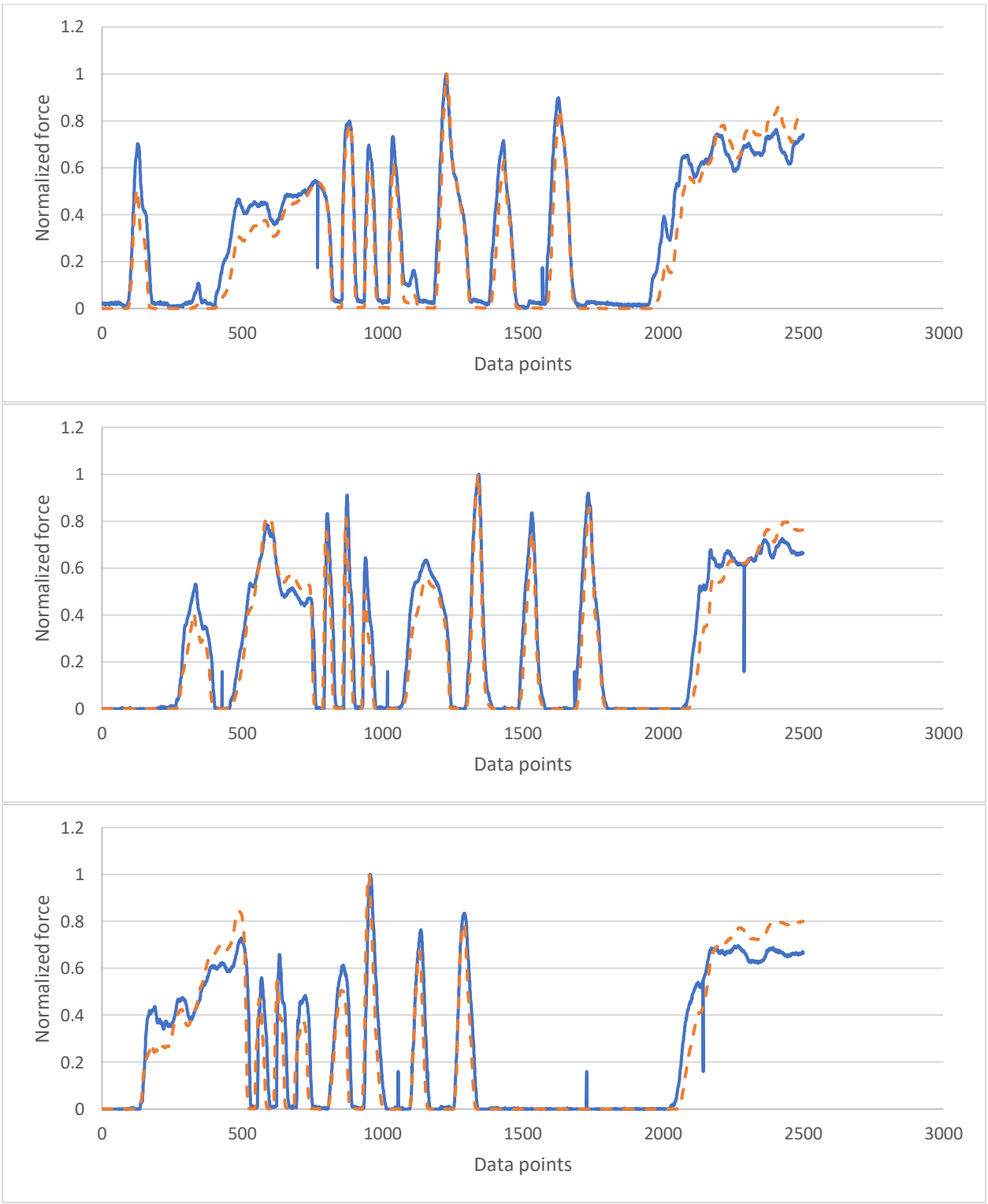

Figure 33. Normalized force data of the dynamic trials, comparing the load cells and the Tekscan sensor. Load cell data is depicted in a solid blue line, Tekscan data is depicted in an orange dashed line.

Chapter 5. METHODOLOGY

5.1 TEST SUBJECT DEMOGRAPHICS

It is our intention to use this device on 10 healthy control subjects and 10 subjects with diabetes. The two groups will be age and sex matched. All test subjects will give informed consent before participating. The test subjects will be between the ages of 18 and 70, and the ethnic and racial composition of the test subject will be similar to the population of Seattle, WA. Exclusion criteria include recent lower limb surgery, inability to ambulate, or pregnancy.

5.2 IDEAL METHODOLOGY

The instrumented footwear study will be conducted in the VA biplane fluoroscopy lab. This study requires a minimum of three trained data collectors—a fourth person may be present to help if needed. The biplane fluoroscopy will be set up to collect gait data of a person walking straight, starting from the north side of the room. The ultrasound machine will be moved to a walkway platform separate from the path that the test subject would take. The placement of the ultrasound machine will be close to the middle of the walking path, on the east side, to allow the test subject to walk the greatest distance possible before being limited by the ultrasound cable length (Figure 34 and Figure 35). The ultrasound clip capture duration will be set to 10 seconds. The laptop responsible for collecting force data will also be placed on the east side of the room. The longer

cable length of the load cells will make it possible for the laptop to be set up outside of the biplane fluoroscopy pit.

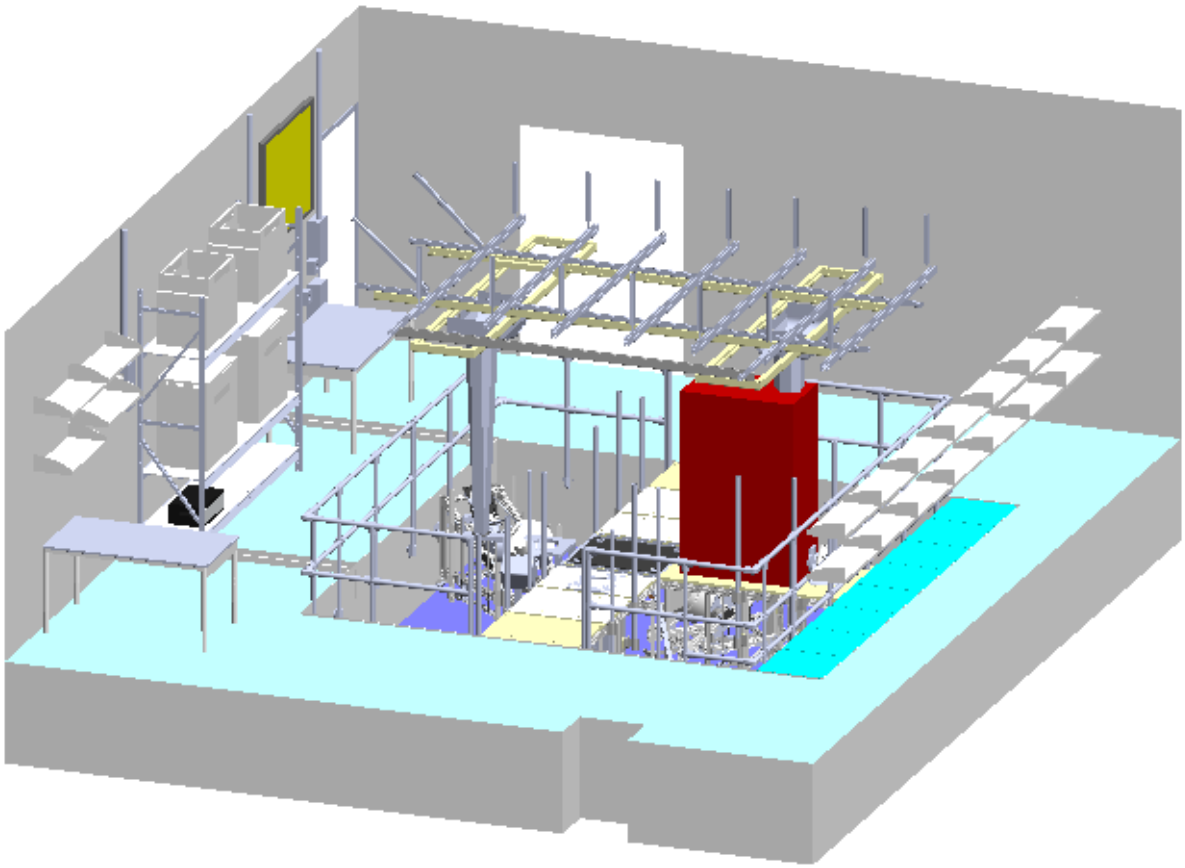

Figure 34. A CAD dimetric view of the biplane fluoroscopy lab, viewing from the south side (north wall visible, yellow board on west wall). This shows a potential setup of the ideal study. The ultrasound machine is depicted as a red box.

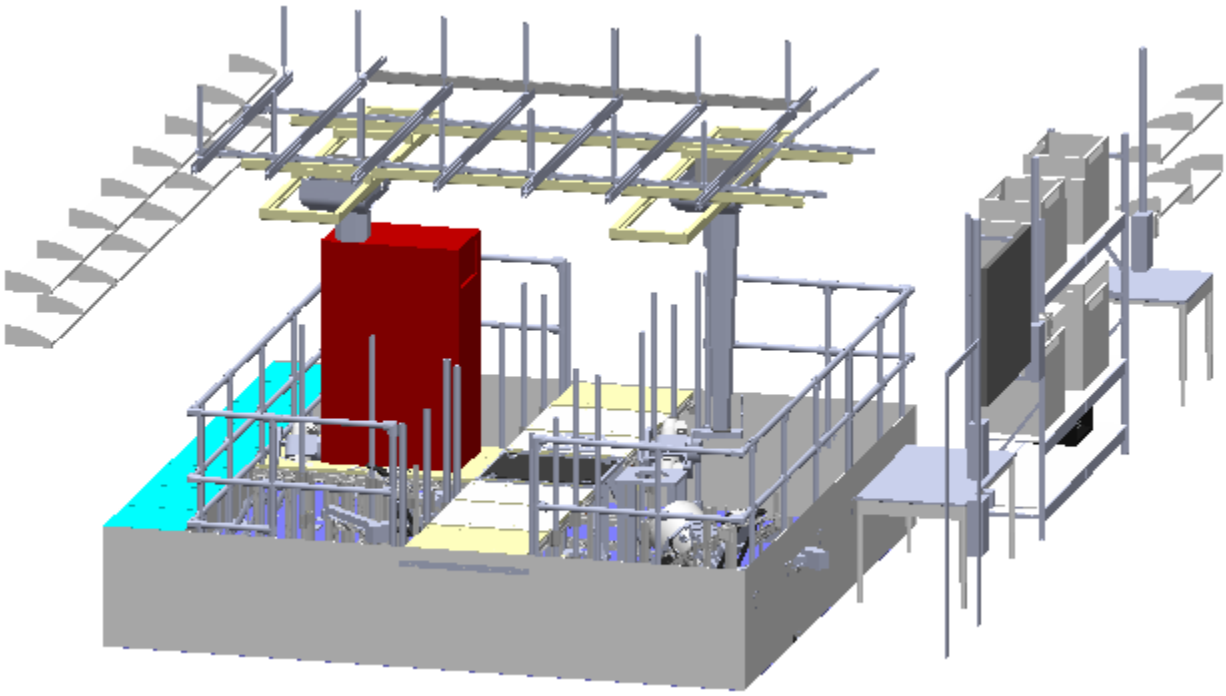

Figure 35. A CAD depicting a potential setup for the study, viewing from the north side (no walls visible). The ultrasound machine is depicted as a red box.

Once all the machines are set up, the test subject will be escorted to the biplane lab. The test subject will remove their footwear and socks. Their feet will be wiped with an alcohol wipe, which may improve ultrasound imaging quality [21]. The instrumented footwear only come in men's sizes 5, 7, 9, and 11; female participants will likely require women's sizes 7 or 9, and will use either men's sizes 5 or 7, respectively. The test subject will receive the properly sized shoe to wear; if their feet fall in between sizes, it is recommended to size down if comfort is acceptable. If sizing down causes too much discomfort, sizing up is possible. However, padding may be required between the foot and shoe straps to ensure the foot is stabilized during ultrasound imaging. The test subject will also wear an accompanying commercial sandal that has a similar build to the instrumented shoe. Without equipping the instrumented shoe yet, the test subject will

make a few practice walks through the biplane fluoroscopy walkway, starting from the north side and walking straight across. The goal of the practice walks is to have the test subject have their left foot land in the imaging field of the biplane fluoroscopy. The practices will help both the test subject and data collector determine the best starting conditions to reduce the number of failed trials.

Two locations, the forefoot (second or third metatarsal head) and the hindfoot (calcaneal tuberosity), will be targeted for data collection. The order of collecting data will be randomized. When collecting data for the calcaneus, the instrumented shoe will have sensors in the heel; in most cases, a neutrally aligned case cover will yield valid data. When collecting data for the metatarsal heads, a few trial-and-errors may be necessary to determine the best forefoot case cover alignments. Once a target location on the foot has been selected, the shoe will be equipped shoe with its sensors. The sensors include four subminiature compression load cells and a disassembled ultrasound probe. The sensors will be accompanied with custom parts that help protect the sensors and hold them in place. The filler material will be placed in the area of the shoe that is currently not in use. A fitted insole material will be placed over the instrumented shoe, leaving a square cutout open at the area collecting data. A sliced gel pad of approximately 5 mm will be cut and placed over ultrasound probe, filling in the cutout of the insole. The test subject will then wear the instrumented shoe, tightening the Velcro to their own comfort, though the fit must be snug enough to prevent the slipping of the foot within the shoe. The test subject will start on the north side of the biplane lab. When instructed, the test subject will lightly tap with their left foot three times and then walk straight across the biplane walkway. The test subject will wait until instructed to go back to the starting position, carefully walking and being mindful of the cables. From here, the process

repeats again until the number of data collection is satisfied, preferably about five trials. Once data collection for one location is complete, repeat the process for the other location on the foot.

5.3 METHODOLOGY FOR FIRST PILOT STUDY

Ideally, the pilot study would have followed the methodology outlined above. However, this was not possible for a few reasons. First, at the time of writing, the Biplane Fluoroscopy Laboratory at the VA Puget Sound (GW11, Building 101) was yet completed. Second, data collection for this thesis was scheduled to take place during an unprecedented pandemic in the spring of 2020. In order to maintain safety for all, recruitment of test subjects has halted. As such, the methodology used for this pilot study was different from the outlined methodology above.

First and foremost, since data were collected on an individual associated with the research study, the VA Puget Sound Institutional Review Board (IRB) determined the results could not be used in any scientific publication but could be presented in this thesis. Secondly, since the biplane fluoroscopy lab was not ready, ambulation occurred on a basic treadmill (Figure 36). While there were no fluoroscopy data to analyze, the treadmill provided greater number of steps to analyze, although the first step of each trial was neglected to avoid inertial factors from a standstill. It was also important to note that walking speed may not have been naturally selected, and that walking speed may have varied across the different trials.

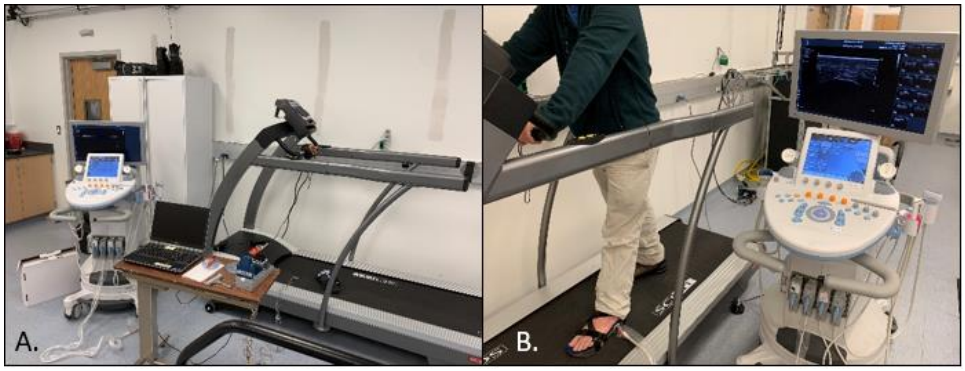

Figure 36. A) Equipment setup for the pilot study. B) Demonstration of using the treadmill.

Data collection for the pilot study started by having the test subject wear the instrumented shoe. For this data collection, heel data were collected first, then the second metatarsal head data. The load cell laptop and the ultrasound machine were set next to the treadmill. Once the instrumented shoe was equipped with its load cells and ultrasound probe, the test subject put on the shoe, strapping the Velcro by themselves to achieve personal comfort. A data collector adjusted the shoe to ensure a snug fit, but the comfort of the test subject was kept in mind. A soft material, typically additional insole material, may be placed on the medial or lateral side of the foot between the shoe straps to help position the foot correctly on the ultrasound probe. There were two people that assisted with data collection. The first person focused on recording force and displacement data. The second person focused on keeping the sensor cables safe. Once the test subject was fitted with the instrumented shoe, they stepped on the treadmill. The test subject walked at a self-selected speed by adjusting a speed setting on the treadmill. The first data collector, when ready, instructed the test subject to begin walking. The load cells and ultrasound machine started recorded at roughly the same time. The ultrasound system was set to capture a clip for 30 seconds. Prior to starting the trial, the test subject's left foot was lifted to offload force on the shoe; it was found empirically that the tightening of the Velcro straps did not have a significant impact on the offloaded load

cells. Once instructed, the test subject will do three quick foot taps outside the track of the treadmill, then begin walking. The purpose of the three foot taps, just like in the dynamic validation test, was to provide a way to align data during analysis. The load cell data recording was manually stopped once the ultrasound clip finished recording. Signs of an unsuccessful trial include interrupted walking or degrading ultrasound imaging quality. Interrupted walking might be caused by shoe discomfort or obstruction caused by sensor cables. Degrading ultrasound quality might be caused by the foot slipping in the shoe or the displacement of the gel pad. From these data, tissue stiffness and EDR was calculated. In the calculation of EDR with the integration method, Excel was used for the majority of the trials—MATLAB version 2018b (MathWorks, Natick, MA) was used to approximate one of the equations for integration, namely the exponential equation of the unloading curve for forefoot trial 3.

5.4 DATA PROCESSING AND ANALYSIS

This thesis does not cover the methodology behind processing biplane fluoroscopy data. Ultrasound data were exported as DICOM files and processed with ImageJ. To calibrate the length measured in ImageJ, a line was drawn between points at a known distance. For the Aixplorer ultrasound clip, depth in increments of 1 cm was provided on the right. Once the line was drawn, the "Analyze" tab was selected, followed by "Set Scale…". In the "Known distance:" box, distance of the drawn line was inputted as 10 mm. The "Unit of length:" does not need to be filled out. The line was displayed at 16.8 pixels/mm. Once the units were set, the shortest vertical distance between the edge of the bone to the outer skin was measured. Each clip was observed frame by frame. With each frame, once the vertical line was drawn, "T" was pressed on the computer keyboard to record the data; this was saved in ImageJ's Region of Interest (ROI) window. To

obtain the length of the drawn line, a recorded frame was selected in the ROI window and "Measure" was pressed. To save the recorded data in the ROI, all the frames had to be selected before saving. There were moments where change in displacement was really small, which made it difficult to track the changes from simply redrawing the vertical line. In these cases, a few frames were skipped to measure a new distance that yields a change. The missing data between two points were filled out with either the mean between two points or interpolation. For cases where the image of the bone seemed to disappear or became too ambiguous to estimate its location, the frame was marked an invalid. These frames were not be used in data analysis. For a given trial, greatest length measured was noted. Displacement data for each frame was determined by subtracting the measured length from the greatest length measured.

The force data were saved as .txt files. The .txt files were opened, and its contents were copied into a spreadsheet, focusing only on the column with the total force; individual load cell forces and timestamps were available if needed. As the ultrasound clips captured at 45 Hz, the force data were resampled down from 100 Hz to 45 Hz. Prior to doing this, the force data was observed for any noise that could affect data accuracy. The noticeable data noise were the random spikes in force data. For a given trial, the force spikes tend to result in the same force value. Spikes were eliminated by taking the mean of its adjacent data points. Once the force data looked acceptable, the interpolation process to resample the data began.

Once the force and displacement data were all sampled at 45 Hz, the data was aligned. However, it was determined empirically that data alignment based on taps/peaks was not optimal, as the resulting force-deformation curve appeared to be inaccurate. One characteristic of an inaccurate

force-deformation curve was unexplainable data trends. For example, a purely vertical line indicated a jump in force with no tissue deformation. Likewise, a purely horizontal line indicated a change in tissue deformation with no influence from force. Timestamps were also unreliable in aligning the data, as the laptop time and the ultrasound system time were not synchronized. In addition, the Aixplorer ultrasound system was not able to properly connect with the cDAQ, which would have made a trigger design possible and therefore allow for a synchronized recording start. For data analysis, it was determined empirically that aligning based on each individual step produced the cleanest force-deformation curve. The individual steps were not be aligned based on peak force and displacement, but rather when the step started. To determine the step start using force data, an averaging technique was used to detect when a step begins or ends. For a given data index, a mean was calculated based on the current data, the previous two points, and the next two points. If the mean value crossed the threshold of 4 N, then that data index was identified as the step start. Determining the step start for the displacement data relied more on subjective observation. Typically, a step began as the displacement data started to consistently increment; this usually began before 1 mm. The step start index of the displacement data was adjusted as needed to obtain the best force-deformation curve. This process was repeated for each step within a given trial. Once all the data in a given trial were aligned, the average of the steps was determined to obtain the average force-deformation curve of a trial. To determine the average, each step data was separated based on the loading portion and the offloading portion, which was marked by the peak force. The end of the loading portion and the beginning of the offloading portion shared the same data index. The greatest number of data points for the loading portion of a step was noted. The maximum data points of the loading portion were used as the value to interpolate other steps' loading portion to achieve the same number of data points. This process was repeated for the

offloading portion. It was important to note that the step with the greatest number of data points in the offloading portion might not have been the same as the one for the loading portion. Once all the steps had the same number of data points for the loading portion and the offloading portion, the average step data for a trial was determined. This was the data used to create the trial's force-deformation curve.

The data to be extracted from a trial were peak displacement, peak force, stiffness, and energy dissipation ratio (EDR). Both peak displacement and force were simply extracted from a trial's entire data set, not its average. The stiffness values and EDR were determined from a trial's average force-deformation curve.

There were two stiffness values to obtain from the force-deformation curve, namely the initial stiffness and the final stiffness [36]. They were determined by observing just the loading curve and separating it into two parts, divided by the curve's inflection point. The initial stiffness was determined by the approximate linear slope from the step's start to the inflection point. The final stiffness was the approximate linear slope from the inflection point to the peak force of the loading curve (Figure 37).

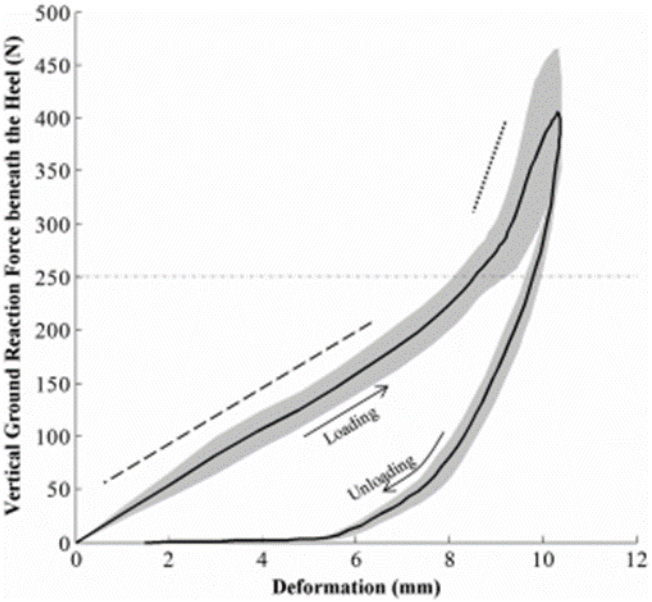

Figure 37. A force-deformation curve with dashed lines indicating different stiffnesses [36].

To standardize the method of determining the slope in this study, the first 20% and last 40% of the loading curve data points were used to calculate the initial and final stiffness, respectively. The reasoning for increasing the number of data points to calculate the final stiffness was to account for the increased number of data points near peak force (Figure 38).

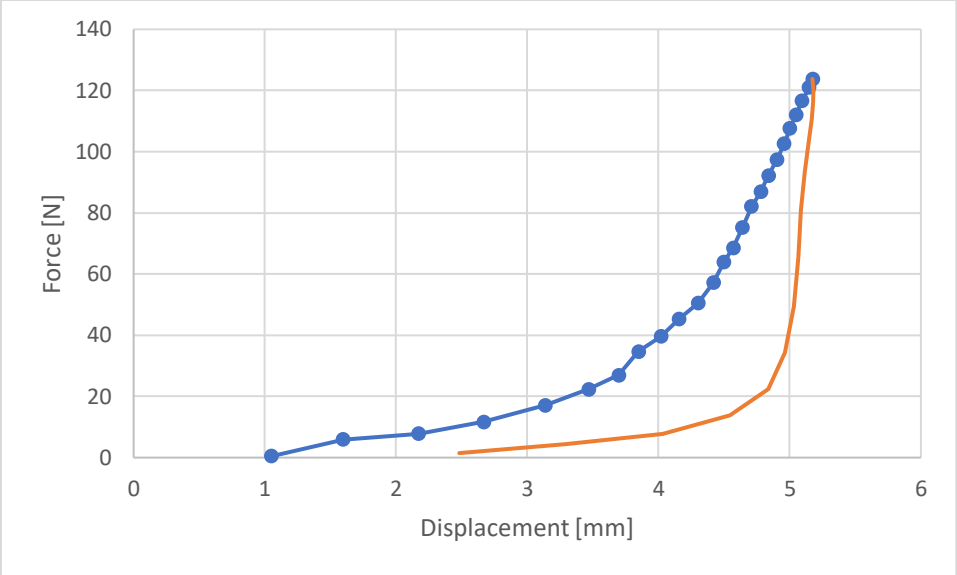

Figure 38. A representative force-deformation curve. In the loading portion of the curve, there are considerably more data points near the peak force.

The EDR informs the energy lost through the plantar soft tissue after force had been applied. The EDR was determined by calculating the area formed by the loop of the force-deformation curve divided by the area under the loading curve. The equation can be expressed as:

$$\mathrm{EDR} = \frac{\mathrm{Area}_{\mathrm{loading}} - \mathrm{Area}_{\mathrm{unloading}}}{\mathrm{Area}_{\mathrm{loading}}}$$

The trapezoidal method was used to calculate the area under the loading curve and the unloading curve. The difference in area of the two curves was the area of the force-deformation loop (Figure 39). Data points with displacement greater than that associated with peak force were neglected. This was to prevent the subtraction of a negative area when finding the difference between the area of the loading curve and unloading curve. The results of the trapezoidal method were verified by using integration on the curves. Approximating a function that closely fits the data set improved

the integration accuracy. Ideally the function was in exponential form, but a polynomial was used if it represented a curve accurately. A disclaimer—the functions determined for integration were used to verify the trapezoidal method and were not intended to explain the data set.

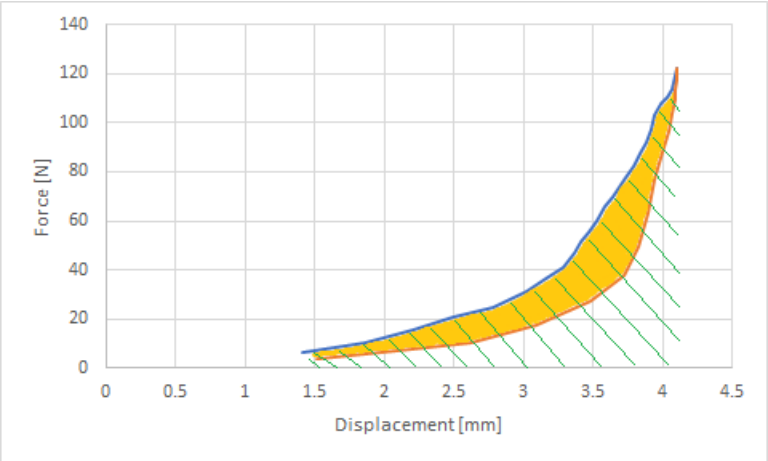

Figure 39. A force-deformation curve depicting the area of the "loop" (yellow area) and the area under the loading curve (green lines).

Chapter 6. PILOT STUDY RESULTS

6.1 ANALYZED DATA

The single test subject in the pilot study was a healthy adult male, weighing 193 lbs. (87.5 kg). The test subject's foot had no abnormalities. Six trials from the pilot study were processed; they were three heel trials and three forefoot (second metatarsal) trials. The ultrasound clips were analyzed frame by frame (Figure 40 and Figure 41). The first step of every trial was excluded from analysis to avoid acceleration effects. Other steps that produced low quality ultrasound data were also excluded (Table 10). From this test, force-deformation curves for the heel (Figure 42) and forefoot (Figure 43) were created. Max deformation, peak force, stiffness, and EDR were determined (Table 11). Integration equations for determining EDR are provided (Table 12).

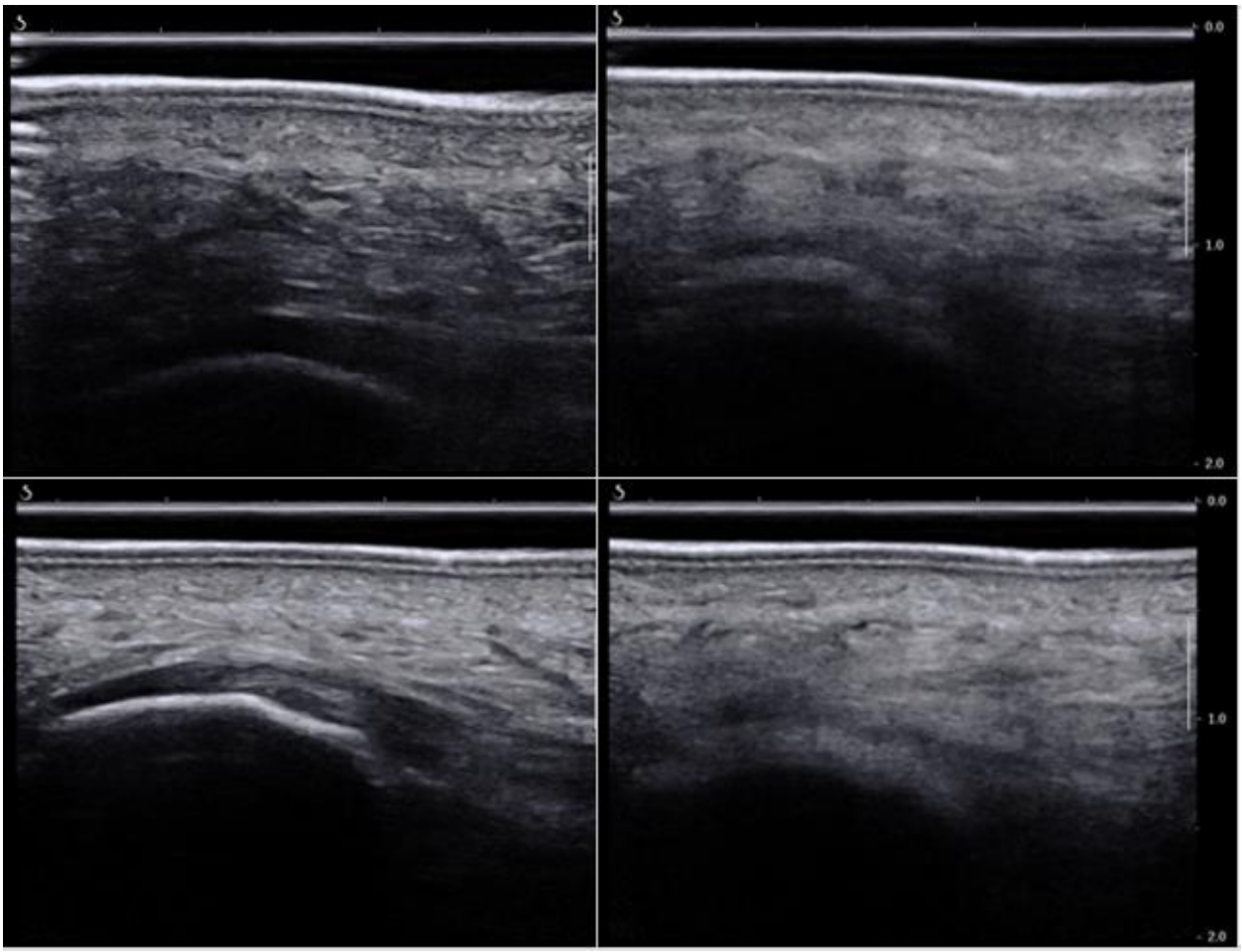

Figure 40. Ultrasound samples of a heel trial. Step start (top left), loading (top right), peak deformation (bottom left), and unloading (bottom right).

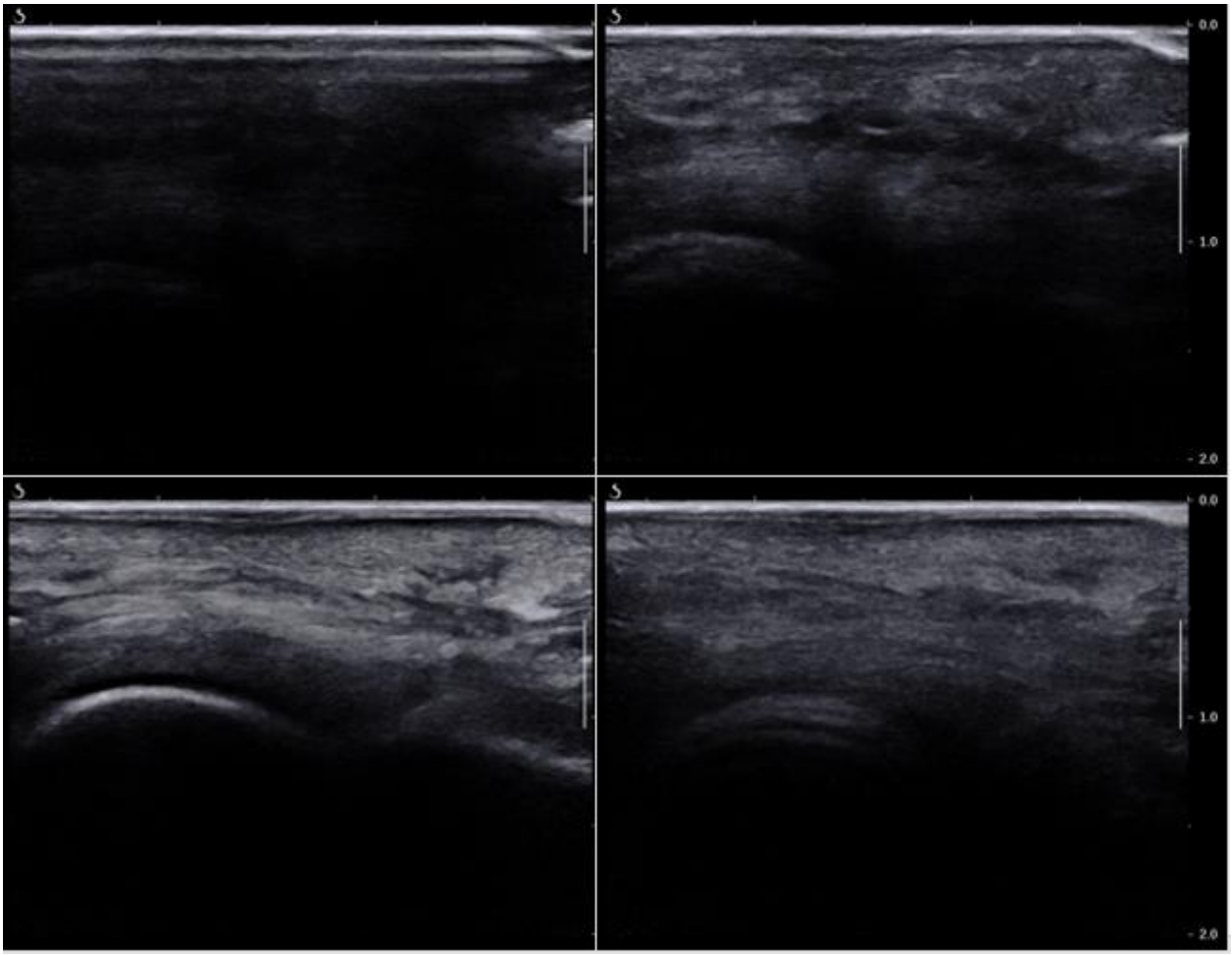

Figure 41. Ultrasound samples of a forefoot trial. Step start (top left), loading (top right), peak deformation (bottom left), and unloading (bottom right).

Table 10. Conditions of each pilot study trial and the steps analyzed.

Trial	Walking Speed (m/s)	Steps Counted	Steps Analyzed
Heel 1	0.447	6	4
Heel 2	0.715	11	10
Heel 3	0.715	10	9
Forefoot 1	1.21	22	21
Forefoot 2	1.21	21	15
Forefoot 3	1.21	21	19

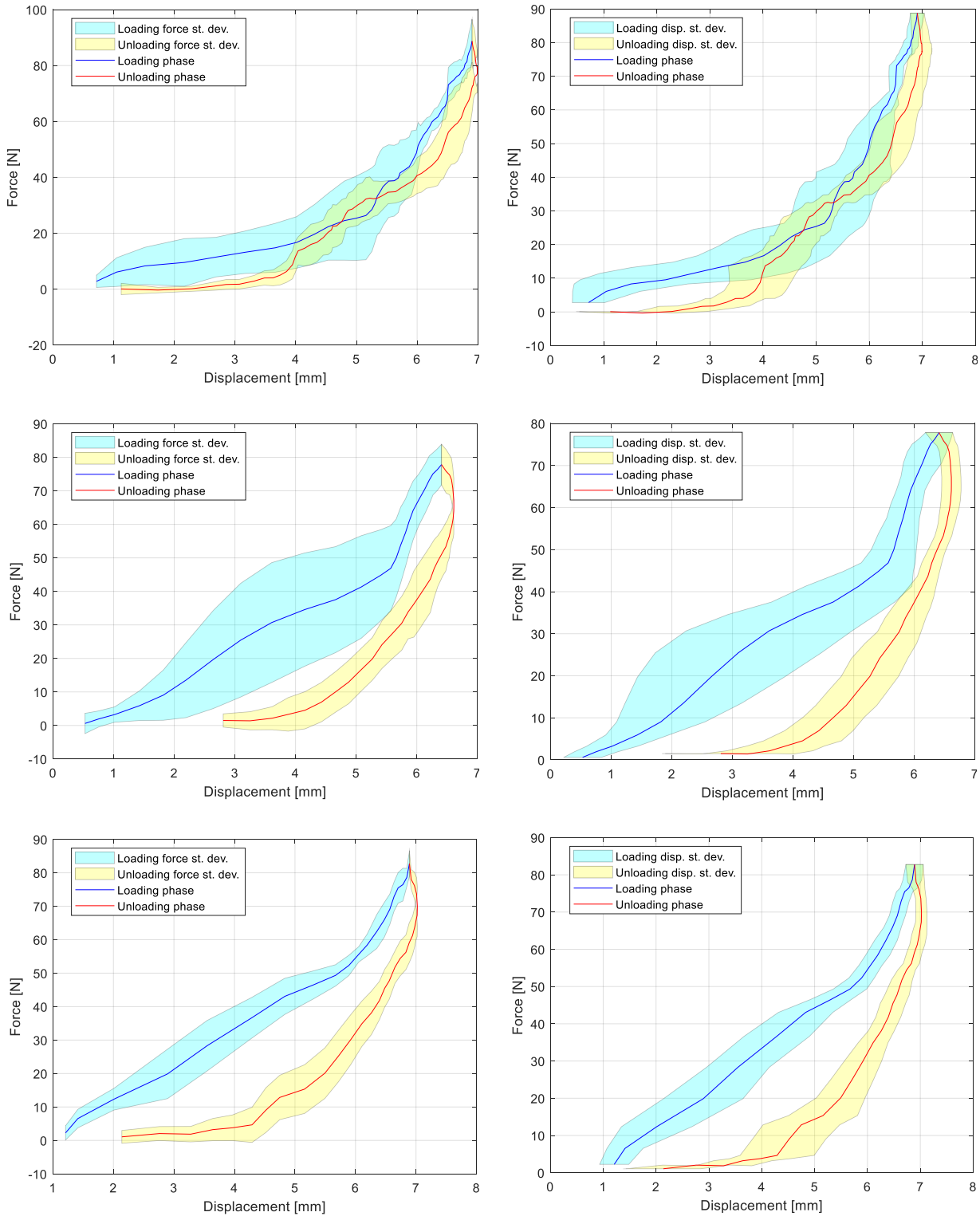

Figure 42. The average force-deformation curves of the three heel trials. Trial 1 starts on the top row. Force standard deviation is on the left column, displacement standard deviation is on the right column.

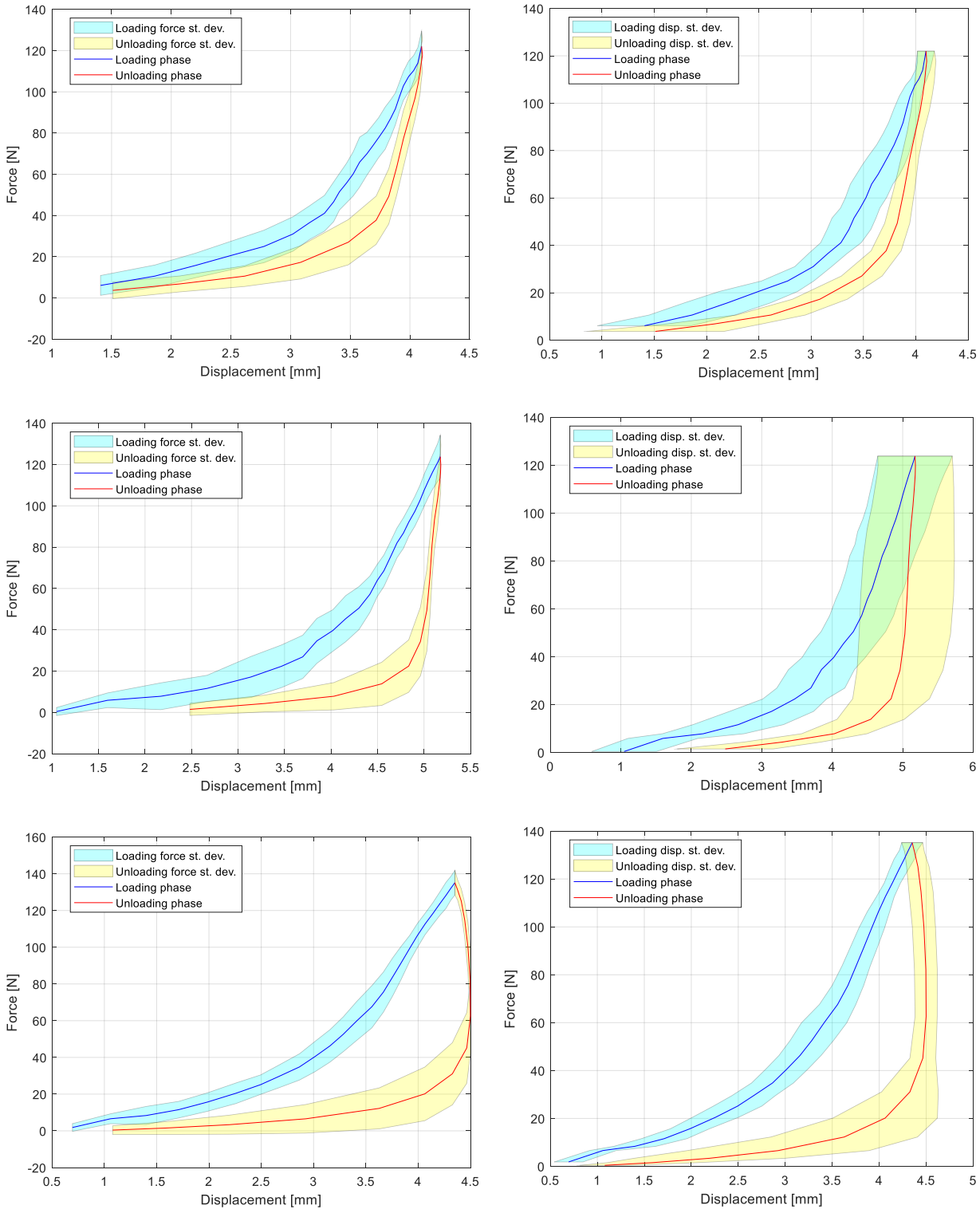

Figure 43. The average force-deformation curves of the three forefoot trials. Trial 1 starts on the top row. Force standard deviation is on the left column, displacement standard deviation is on the right column.

Table 11. Pilot study data. The forefoot only looks at the second metatarsal head.

Test variable		Test location	Trial 1	Trial 2	Trial 3	Average (S.D.)
Max deformation [mm]		Heel	8.11	7.87	8.11	8.03 (0.14)
		Forefoot	4.29	6.20	4.76	5.08 (1.00)
Peak force [N]		Heel	95.8	86.1	88.8	90.2 (5.00)
		Forefoot	136	139	149	141 (7.08)
Stiffness [N/mm]	Initial	Heel	5.32	6.54	10.5	7.44 (2.69)
	Final		45.1	35.7	37.7	39.5 (4.95)
	Initial	Forefoot	13.8	8.00	10.7	10.8 (2.90)
	Final		123	89.7	86.3	99.6 (20.2)
EDR	Trapezoidal	Heel	0.30	0.69	0.63	0.54 (0.21)
	Integration		0.26	0.68	0.63	0.52 (0.23)
	Trapezoidal	Forefoot	0.42	0.71	0.81	0.65 (0.20)
	Integration		0.44	0.69	0.83	0.65 (0.20)

Table 12. Equation used for integration to approximate the EDR of the pilot study trials.

Test and trial number	Curve type	Equation [bounds]	R^2
Heel 1	Loading	$y = 2.68e^{0.491x}$ [0.715, 6.921]	0.973
	Unloading	$y = 3.309x^2 - 14.69x + 16.16$ [1.12, 6.98]	0.963
Heel 2	Loading	$y = 0.402x^4 - 4.927x^3 + 20.31x^2 - 22.33x + 8.480$ [0.528, 6.485]	0.995
	Unloading	$y = 0.058e^{1.075x}$ [2.807, 6.611]	0.984
Heel 3	Loading	$y = 0.115x^5 - 2.069x^4 + 14.12x^3 - 45.03x^2 + 76.99x - 45.27$ [1.209, 6.891]	0.999
	Unloading	$y = 0.138e^{0.894x}$ [2.139, 7.022]	0.987
Forefoot 1	Loading	$y = 10.75x^3 - 66.89x^2 + 147.16x - 99.06$ [1.407, 4.098]	0.999
	Unloading	$y = 17.47x^5 - 226.37x^4 + 1152.6x^3 - 2871.9x^2 + 3496.9x - 1657.1$ [1.511, 4.098]	0.997
Forefoot 2	Loading	$y = 4.098x^3 - 27.22x^2 + 63.26x - 41.52$ [1.049, 5.175]	0.999
	Unloading	$y = 0.017e^{1.635x}$ [2.482, 5.181]	0.906
Forefoot 3	Loading	$y = -0.636x^4 + 10.15x^3 - 36.92x^2 + 58.26x - 24.70$ [0.70, 4.38]	0.999
	Unloading	$y = -0.921e^{3.871x} + 0.916e^{3.875x} + 5.871$ [0, 2.6986]	0.976

6.2 DISCUSSION

The force-deformation curve created by the Ultrashoe indicates hysteresis. The shape of the force-deformation curve is similar to other curves in literature [19, 21, 36, 37]. One important distinction to make on the curves formed from the pilot study is the slight increase of tissue displacement

during the first moments of unloading; this is apparent in some of the trials. This increase in displacement is not seen in other literature. While it is possible this phenomenon is indicating some sort of inertial effects of force imparted onto the tissue, the cause is most likely due to the design of the shoe and its data collection, specifically the manual alignments of the force and displacement data.

For plantar soft tissue displacement, the Ultrashoe obtained average values of 8.03 mm and 5.08 mm at the heel and forefoot, respectively. Telfer et al. reported a heel deformation of 5.7 mm. The method of collecting data was similar to the Ultrashoe in that an ultrasound probe was embedded in the heel area. There were 16 test subjects in this study [33]. Wearing et al. reported a heel deformation of 10.3 mm. The results were collected by using lateral radiography and a pressure plate that sampled at 50 Hz. There were 16 test subjects in this study [36]. Cavanagh measured the second metatarsal head with ultrasonography and reported a deformation of 7.0 mm. This data was collected by using an embedded ultrasound sensor within a floor and having test subjects step in a target area, though this was not true ambulation. There were 5 test subjects in this study [27]. As this thesis only had one test subject, it is difficult to make a conclusion based on the trends. The amount of deformation also depends on the initial thickness of the tissue; thicker feet will have the potential for more deformation. Initial thickness was not controlled between these subjects.

The Ultrashoe provided an average peak force of 90.2 N and 141 N for the heel and forefoot, respectively. The area of the ultrasound probe face was approximately 188 mm^2, inferred by a CAD model provided by SSI. Therefore, the peak pressure of the heel and forefoot is 481 kPa and 752 kPa, respectively. In a study by Ledoux et al. that looked at plantar force distribution based

on body weight (BW), it was found that peak force at the calcaneus and second metatarsal head were 0.962 BW and 0.138 BW, respectively, for a neutrally aligned foot. This study involved 11 test subjects with neutrally aligned feet. The pressure plate in Ledoux et al.'s study comprised of 2048 sensors of area 25 mm^2 and sampled at 28 Hz. There were 73.6 sensors counted in the heel location, giving it an area of 1840 mm^2. There were 30.1 sensors in the second metatarsal head location, giving it an area of 752.5 mm^2 [38]. The BW/mm^2 for the heel and forefoot was 5.23 x 10^{-4} and 1.83 x 10^{-4}. The test subject in this thesis had a BW of 859 N. Using the peak force obtained from the Ultrashoe, the peak forces described by the test subject's BW for the heel and second metatarsal head are 0.105 BW and 0.164 BW, respectively. Given the area of the ultrasound probe surface, the respective BW/mm^2 of the heel and forefoot are 5.59 x 10^{-4} and 8.72 x 10^{-4}. When comparing the Ultrashoe's force per area to Ledoux et al.'s, the heel data seems accurate. In Wearing et al.'s study, a peak force of 411 N at the heel was reported, However, the data also came from a pressure mat and included the complete area of the heel. The force data from the Ultrashoe comes from the force imparted on the face of the ultrasound probe. If the area of the heel is approximated similarly with Ledoux et al.'s results, then the peak pressure of heel in Wearing et al.'s study was 249 kPa. This is less than what was calculated for the heel peak pressure for this thesis.

The initial and final stiffness of the heel were 7.44 N/mm and 39.5 N/mm, respectively. The initial and final stiffness of the forefoot were 10.8 N/mm and 99.6 N/mm, respectively. The study by Wearing et al. yielded heel initial and final stiffnesses of 32.0 N/mm and 211.7 N/mm, respectively [36]. It is important to keep in mind that these stiffness values came from the forces output by the

entire heel, whereas the Ultrashoe study only picks up the force imparted on the face of the ultrasound probe.

The Ultrashoe reported the EDR at the heel as 0.540, and the forefoot as 0.648. Telfer et al. reported an EDR of 0.54 at the heel [33].Wearing et al. reported an EDR of 0.66 at the heel [36]. Hsu et al. reported an EDR of 0.587 at the second metatarsal head for a control group. In Hsu et al.'s study, an ultrasound device equipped with a miniature load cell to press into test subjects' feet in a supine position, from which EDR was obtained. Eight healthy subjects participated in this study [21].

In general, the data obtained from the Ultrashoe are on the same order of magnitude of the results found in literature. However, the comparison of peak force and stiffness data to the literature here is challenging because of the different plantar area captured for force data. For trends, the Ultrashoe showed that the tissue displacement is greater at the heel than the forefoot. The Ultrashoe also showed that the EDR at the heel is lower than the forefoot. However, these trends cannot be compared to literature. The studies referenced in the discussion that involved tissue displacement and EDR only focused on either the heel or forefoot, not both. In addition, this thesis only had one test subject. So, while having one test subject helps with observing the performance of the Ultrashoe, it is difficult to draw conclusions on trends noticed from data collection.

The data obtained from the Ultrashoe show promising results. Given the unique approach to collecting in vivo plantar soft tissue data, there are some flaws and limitations to its design. One of the limitations of the instrumented shoe is its inability to collect synchronous displacement and force data. By having to collect data separately and process one set of data to match the other can

introduce error to the analysis. Another limitation is maintaining consistent lockdown of the foot. Improved lockdown can reduce the number of unusable ultrasound frames due to low image quality or loss of contact. A flaw to the instrumented shoe is its durability. Even with using quality resin material from the Stratasys Objet 350, it is possible to break the shoe, as it had happened during the pilot data collection. The break in the shoe was caused by the tightening of the shoe straps. Although this break likely did not affect prior data collection, it does show that the shoe needs to be better designed for improved durability. In addition, one of the load cell cables ripped apart. This occurred after data collection for the pilot study. This break suggests that a better cable strain relief must be designed (Figure 44). An immediate and effective solution is to handle the shoe with greater care. A future limitation is the length of the ultrasound cable that will limit the number, and potentially the quality, of the steps in the biplane lab. Cable length was not an issue for the pilot data when walking on the treadmill.

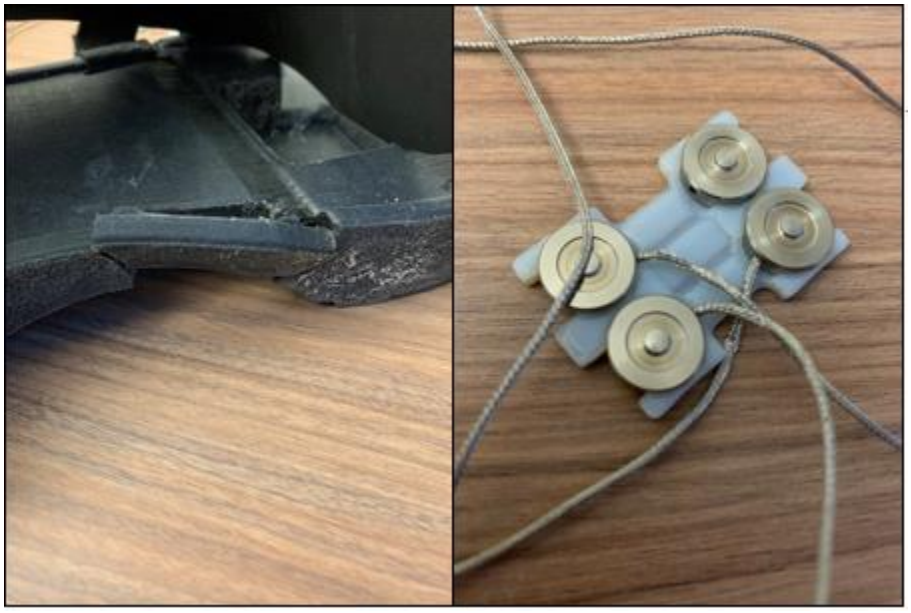

Figure 44. Mechanical failures of the shoe. The area where the shoe strap goes through broke (left) and the load cell cable on top ripped out (right).

Chapter 7. CONCLUSION

The goal of the thesis was to design and develop an instrumented shoe capable of collecting dynamic plantar soft tissue force and deformation data while walking. The instrumented footwear collects data at plantar areas that are at high risk for ulcerations, namely the heel and forefoot [9].

This thesis provided insight on the possibilities of collecting in vivo gait data. However, having more than one test subject would help provide more insight to the effectiveness of the shoe. The force and displacement data were processed to produce successful force-deformation curves that demonstrated hysteresis, a characteristic indicating viscoelastic properties within the plantar fat pads. Some of the tissue properties measured by the Ultrashoe were similar to the literature, namely the deformation and EDR. It was challenging to make comparisons that involved force, since the force detected in the heel of the Ultrashoe was only a small part of the entire heel pad. Concerns of collecting inaccurate data could be alleviated by addressing some of the Ultrashoe limitations. Some of the limitations include asynchronous data collection, shoe lockdown and durability, and the tethering to the ultrasound machine.

Acknowledging the limitations of the current iteration of the Ultrashoe, there are future improvements the shoe could see to enhance its overall performance. The LV code and the hardware could be reconfigured to make synchronized data collection possible. The main reasons why synchronized data collection was not possible was the inability to trigger the Aixplorer ultrasound system with a signal. While it may be possible to have the cDAQ manage both the trigger of the ultrasound and the data collection of the load cells, it is recommended that the data collection control be migrated from the cDAQ-9178 to a compact reconfigurable input-output

(cRIO) system. The recommended chassis, of which the CLiMB lab already possesses, is the cRIO-9067, an 8-slot chassis that can process the data acquisition real time. The advantage of upgrading to the cRIO, more specifically the cRIO-9067, is the improved performance in sampling rate and control robustness. The cDAQ can be thought of as a unidirectional data flow, such that the cDAQ is optimized for either only collecting data or outputting signals. The cRIO can handle both input and output of signals simultaneously with no concern for performance.

The current design of the Ultrashoe is able to collect data successfully, but its build can be improved upon which would ultimately help with the quality of data. While 3D printing provides the capability to create unique shoe designs, the materials used in 3D printing are marketed as use for prototype. To improve durability, the shoe design should be updated to have more material where the strap slots are—this design recommendation is especially important if maintaining the 3D printing route.

One different method of shoe development to explore is the use of silicone molding, which can lead to a more robust shoe. In addition, the shoe straps in the current design were sewn by either hand or machine. Although the straps and Velcro in the shoe have worked, they were not necessarily comfortable, and the fit was not always optimal, even with the ability to change fit with the Velcro. It is recommended that future creation of the shoe be assisted by a cobbler to ensure an improved fit.

The ultrasound cable is the limiting cable length, measuring about 2m. The load cell cable length is approximately 6.1m. The short ultrasound cable may affect gait, even in the biplane walkway.

When the Ultrashoe is used in testing outside of the biplane lab, using a treadmill may be an option if extended walking is required. For future improvements, a better design in strain relief of the sensor cables is highly recommended. Having a lab personnel to help spot the cables during data collection is helpful. However, having better strain relief design adds in another safety outlet if a trial goes wrong; this is especially important should a cable spotter is not present. The load cell cables are more fragile than the ultrasound cable, but the cost to replace a load cell is significantly less than the ultrasound probe. An idea to explore in the future is the use of wireless ultrasound. Although there are concerns for its capture frame rate and potential latency issues, a wireless ultrasound would remove the concerns of being tethered to an ultrasound machine. Unfortunately, there seems to be little in literature on the use of wireless ultrasound in biomechanical studies, making it difficult to justify its use.

Lastly, digital image correlation (DIC) should be explored as a method to measure soft tissue displacement. The current method of using ImageJ to go through ultrasound clips frame by frame is an acceptable method to calculate vertical displacement of the tissue, but it is a time-consuming process. Using DIC technique will help make the displacement analysis process more efficient. It may also help illuminate findings on how the whole soft tissue deforms. Use of DIC on ultrasound images for biological tissue has been done before and has shown promises of providing accurate data [39, 40]. A few DIC software have been explored to see what works best with ultrasound images; the software by LaVision (Göttingen, Germany) has shown promise. However, further exploration of different DIC software is encouraged.

In this thesis, the Ultrashoe has shown that it can collect comprehensible data, and areas for further improvement have been identified. If the Ultrashoe continues to improve, it can become a reliable instrument to collect in vivo plantar soft tissue data. The Ultrashoe can help provide greater understanding to the changes in plantar soft tissue properties for those with diabetes. Although the current scope of the Ultrashoe is to have it be used as a research tool, it is possible for it to become an instrument for clinicians to use. Clinicians can use the shoe to help people with diabetes determine if they need treatment such as diabetic footwear. The Ultrashoe could also help in guiding the design of future diabetic footwear by providing insight on areas of the feet that sustain high levels of pressure.

BIBLIOGRAPHY

[1] E. S. Huang, M. O'Grady, A. Basu and J. C. Capretta, "Projecting the Future Diabetes Population Size and Related Costs for the U.S.," *Diabetes Care,* vol. 32, no. 12, pp. 2225-2229, 2009.

[2] W. Yang, T. M. Dall, K. Beronjia, J. Lin, A. P. Semilla, R. Chakrabarti and P. F. Hogan, "Economic Costs of Diabetes in the U.S. in 2017," *Diabetes Care,* vol. 41, no. 5, pp. 917-928, 2018.

[3] Center for Disease Control and Prevention, "National Diabetes Statistics Report," U.S. Department of Health and Human Services, Washington, D.C., 2020.

[4] Y. Liu, S. Sayam, X. Shao, K. Wang, S. Zheng, Y. Li and L. Wang, "Prevalence of and Trends in Diabetes Among Veterans, United States, 2005-2014," *Preventing Chronic Disease,* vol. 14, no. E135, pp. 1-5, 2017.

[5] S. Pai and W. R. Ledoux, "The compressive mechanical properties of diabetic and non-diabetic plantar soft tissue," *Journal of Biomechanics,* vol. 43, no. 9, pp. 1754-1760, 18 June 2010.

[6] S. Pai and W. R. Ledoux, "The shear mechanical properties of diabetic and non-diabetic plantar soft tissue," *Journal of Biomechanics,* vol. 45, no. 2, pp. 364-370, 10 January 2012.

[7] D. G. Armstrong, A. J. Boulton and S. A. Bus, "Diabetic Foot Ulcers and Their Recurrence," *The New England Journal of Medicine,* vol. 376, no. 24, pp. 2367-2375, 15 June 2017.

[8] M. Ibrahim, R. El Hilaly, M. Taher and A. Morsy, "A pilot study to assess the effectiveness of orthoic insoles on the reduction of plantar soft tissue strain," *Clinical Biomechanics,* vol. 28, no. 1, pp. 68-72, 2012.

[9] S. Pai and W. R. Ledoux, "The Quasi-Linear Viscoelastic Properties of Diabetic and Non-Diabetic Plantar Soft Tissue," *Annals of Biomedical Engineering,* vol. 39, no. 5, pp. 1517-1527, 2011.

[10] F. Crawford, G. Cezard and F. M. Chappell, "The development and validation of a multivariable prognostic model to predict foot ulceration in diabetes using a systematic review and individual patient data meta-analyses," *Diabetic Medicine,* vol. 35, pp. 1480-1493, 18 August 2018.

[11] J. W. Walsh, O. J. S. M. O. Hoffstad and D. J. Margolis, "Association of diabetic foot ulcer and death in a population-based cohort from the United Kingdom," *Diabetic Medicine,* vol. 33, no. 11, pp. 1493-1498, 2016.

[12] P. R. Cavanagh, "Therapeutic footwear for people with diabetes," *Diabetes/Metabolism Research and Reviews,* vol. 20, no. Suppl 1, pp. S51-S55, 2004.

[13] S. A. Bus, "Foot structure and footwear prescription in diabetes mellitus," *Diabetes/Metabolism Research and Reviews,* vol. 24, no. Suppl 1, pp. S90-S95, 2008.

[14] A. Ersen, L. S. Adams, R. T. H. G. B. Myers, L. A. Lavery and M. Yavuz, "Temperature Regulating Shoes for Prevention of Diabetic Foot Ulcers," *Diabetes,* vol. 67, no. Suppl 1, July 2018.

[15] T. M. Owings, J. L. woerner, J. D. Frampton, P. R. Cavanagh and G. Botek, "Custom Therapeutic Insoles Based on Both Foot Shape and Plantar Pressure Measurement Provide Enhanced Pressure Relief," *Diabetes Care,* vol. 31, no. 5, pp. 839-844, 2008.

[16] C. E. Dombroski, M. E. Basldon and A. Froats, "The use of a low cost 3D scanning and printing tool in the manufacture of custom-made foot orthoses: a preliminary study," *MNC Research Notes,* vol. 7, no. 443, 2014.

[17] S. Telfer, J. Pallari, J. Munguia, K. Dalgarno, M. McGeough and J. Woodburn, "Embracing additive manufacture: implications for foot and ankle orthosis design," *BMC Musculoskeletal Disorders,* vol. 13, no. 84, 2012.

[18] M. Yarwindran, N. Azwani Sa'aban, M. H. I. Ibrahim and R. Periyasamy, "Thermoplastic Elastomer Infill Pattern Impact on Mechanical Properties 3D Printed Customized Orthotic Insole," *ARPN Journal of Engineering and Applied Sciences,* vol. 11, no. 10, pp. 6519-6524, May 2016.

[19] S. C. Wearing, J. E. Smeathers, B. Yates, S. R. Urry and P. Dubois, "Bulk compressive properties of the heel fat pad during walking: A pilot investigation in plantar heel pain," *Clinical Biomechanics,* vol. 24, no. 2009, pp. 397-402, 2009.

[20] D. De Clercq, P. Aerts and M. Kunnen, "The Mechanical Characteristics of the Human Heel Pad During Foot Strike in Running: An In Vivo Cineradiographic Study," *Journal of Biomechanics,* vol. 27, no. 10, pp. 1213-1222, 1994.

[21] C.-C. Hsu, W.-C. Tsai, Y.-W. Shau, K.-L. Lee and C.-F. Hu, "Altered energy dissipation ratio of the plantar soft tissues under the metatarsal heads in patients with type 2 diabetes mellitus: A pilot study," *Clinical Biomechanics,* vol. 22, no. 2007, pp. 67-73, 2007.

[22] D. Lemmon, T. Y. Shiang, A. Hashmi, J. S. Ulbrecht and P. R. Cavanagh, "The Effect of Insoles in Therapeutic Footwear -- A Finite Element Approach," *Journal of Biomechanics,* vol. 30, no. 6, pp. 615-620, 1997.

[23] M. J. Young, C. J, T. PM and A. J. Boulton, "Weight bearing ultrasound in diabetic and rheumatoid arthritis patients," *The Foot,* vol. 5, no. 2, pp. 76-79, 1995.

[24] D. J. Parker, G. Cooper, S. Pearson, G. Crofts, D. J. Howard, J. Busby and C. J. Nester, "A device for characterising the mechanical properties of the plantar soft tissue of the foot," *Medical Engineering and Physics,* vol. 37, no. 11, pp. 1098-1104, 2015.

[25] K. Matsubara, T. Matsushita, Y. Tashiro, S. Tasaka, T. Sonoda, Y. Nakayama, Y. Yokota, Y. Suzuki, M. Kawagoe and T. Aoyama, "Repeatability and agreement of ultrasonography with computed tomography for evaluating forefoot structure in the coronal plane," *Journal of Foot and Ankle Research,* vol. 10, no. 17, 2017.

[26] K. Rome, R. Campbell, A. Flint and I. Haslock, "Reliability of weight-bearing heel pad thickness measurements by ultrasound," *Clinical Biomechanics,* vol. 13, pp. 374-375, 1998.

[27] P. R. Cavanagh, "Plantar soft tissue thickness during ground contact in walking," *Journal of Biomechanics,* vol. 32, no. 6, pp. 623-628, 1999.

[28] J. M. Iaquinto, R. Tsai, D. R. Haynor, M. J. Fassbind, B. J. Sangeorzan and W. R. Ledoux, "Marker-based validation of a biplane fluoroscopy system for quantifying foot kinematics," *Medical Engineering & Physics,* vol. 36, no. 3, pp. 391-396, 2014.

[29] D. G. Nishimura, Principles of Magnetic Resonance Imaging, 1st ed., Lulu, 2010.

[30] Medical Imaging & Technology Alliance, "Modalities," National Electrical Manufacturers Association, 6 June 2010. [Online]. Available: https://www.medicalimaging.org/about-mita/medical-imaging-primer/. [Accessed 28 October 2019].

[31] B. A. Lipsky, "Osteomyelitis of the Foot in Diabetic Patients," *Clinical Infectious Disease,* vol. 25, no. 6, pp. 1318-26, 1997.

[32] J. M. Iaquinto, M. W. Kindig, D. R. Haynor, Q. Vu, N. Pepin, R. Tsai, B. J. Sangeorzan and W. R. Ledoux, "Model-based tracking of the bones of the foot: A biplane fluoroscopy validation study," *Computers in Biology and Medicine,* vol. 92, pp. 118-127, 2018.

[33] S. Telfer, J. Woodburn and D. E. Turner, "Measurement of functional heel pad behaviour in-shoe during gait using orthotic embedded ultrasonography," *Gait & Posture,* vol. 39, no. 2014, pp. 328-332, 2013.

[34] Stratasys, "What is PolyJet Technology?," Stratasys Ltd., 2019. [Online]. Available: https://www.stratasys.com/polyjet-technology. [Accessed 28 October 2019].

[35] K. R. Parham, C. C. Gordon and C. K. Bensel, "Anthropometry of the Foot and Lower Leg of U.S. Army Soldiers: Fort Jackson, SC -- 1985," US Army Natick RD&E Center, Natick, 1992.

[36] S. C. Wearing, S. L. Hooper, P. Dubois, J. E. Smeathers and A. Dietze, "Force-Deformation Properties of the Human Heel Pad during Barefoot Walking," *Medicine & Science in Sports & Exercise,* vol. 46, no. 8, pp. 1588-1594, 2014.

[37] M. B. Bennett and R. F. Ker, "The mechanical properties of the human subcalcaneal fat pad in compression," *Journal of Anatomal* , pp. 131-138, 1990.

[38] W. R. Ledoux and H. J. Hillstron, "The distributed plantar vertical force of neutrally aligned and pes planus feet," *Gait and Posture,* vol. 15, no. 1, pp. 1-9, 2002.

[39] J.-S. Affagard, P. Feissel and S. F. Bensamoun, "Measurement of the quadriceps muscle displacement and strain fields with ultrasound and Digital Image Correlation (DIC) techniques," *Innovation and Research in BioMedical engineering,* vol. 36, no. 3, pp. 170-177, 2015.

[40] G. Okotie, S. Duenwald-Kuehl, H. Kobayashi, M.-J. Wu and R. Vanderby, "Tendon Strain Measurements With Dynamic Ultrasound Images: Evaluation of Digital Image Correlation," *Journal of Biomechanical Engineering,* vol. 134, no. 2, pp. 1-4, 2012.

[41] SuperSonic Image, "SuperSonic Image," [Online]. Available: https://www.supersonicimagine.com/Instruction-for-use-Aixplorer-R. [Accessed 25 March 2019].

[42] D. G. Armstrong and L. A. Lavery, "Diabetic Foot Ulcers: Prevention, Diagnosis and Classification," *American Family Physician,* vol. 57, no. 6, pp. 1325-1332, 15 March 1998.

[43] J. W. Klaesner, M. K. Hastings, D. Zou, C. Lewis and M. J. Mueller, "Plantar Tissue Stiffness in Patients With Diabetes Mellitus and Peripheral Neuropathy," *Archives of Physical Medicine and Rehabilitatoin,* vol. 83, no. 12, pp. 1796-1801, 2002.

APPENDICES

APPENDIX A: ULTRASOUND INSTRUCTIONS AND OPTIMAL SETTINGS

When turning on the Aixplorer, ensure that the appropriate transducer is selected. Start by pressing "Probe" on the Aixplorer knob interface, located near the top left area. On the touch screen menu, a list of transducers will be listed. Find the appropriate SLH20-6 probe and select "Foot-Ankle" as the preset option. If there are more than one SLH20-6 probe connected to the ultrasound system, the order of the available probes on the touch screen interface corresponds with the order of the ultrasound hardware connection. Be sure to select the probe on the touch screen that corresponds to the disassembled probe. Below are the recommended settings used in data capture for the calcaneus and metatarsal heads, and explanations are provided (Table A1). The highest achievable frame rate is prioritized, followed by the quality of the image. The method of obtaining optimal quality images is subjective and will ultimately be up to the data collector to select ultrasound settings to their preference. However, it is important to be mindful of the image frame rate. It was found by trial-and-error that the settings can optimize the SLH20-6 frame rate up to 45 Hz. The settings should not result in a capture rate lower than 45 Hz unless it is justifiable. The Aixplorer manual also provides an explanation of the settings [41].

Table A1. Optimal settings of the Aixplorer ultrasound machine along with reasoning.

Settings	Selected Option	Reasoning
Harmonic imaging	Off	Harmonic imaging is best used to reduce backscattered attenuation, a phenomenon likely to occur when imaging through the ribs. Turning this feature on is not beneficial regarding foot tissue imaging, and also reduces the system's frame rate.
SuperCompound	On	These feature "provides superior texture, enhanced edge delineation and reduces shadowing." [41] Turning on this feature also helps to maximize the frame rate.
Res / Gen / Pen	Res	Choosing "Res" provides the highest resolution of the image possible. The frequency is such that superficial images are made clearer. Generally, using "Pen" could yield a higher frame rate, but based on these settings, the highest frame rate of 45 Hz is already achieved. As such, the "Res" option was selected to provide better image quality without any real reduction in frame rate.
HD / Fr. Rate	Med	"Med" was chosen over "HD" because it helps make the images look grainy, a feature that may help with Digital Image Correlation (DIC), although DIC is not used in this thesis. Med was chosen over "Fr. Rate" because when "Fr. Rate" is chosen the ultrasound image looked like it had some artefacts (depending on other settings). For the provided setting selection here, choosing "Fr. Rate" does not provide a higher frame rate.
Zoom	Custom HD Zoom (see reasoning)	The Aixplorer features two zoom options: "Digital Zoom" and "HD Zoom". Digital Zoom is simply the magnification of the image seen on the

		screen—this can be done on either live images or post-processing. Digital Zoom does not affect the system's frame rate. HD Zoom allows the transducer to focus on a certain part of the image during live imaging. This could lead to better resolution in the area of interest. The following instructions show how to set up the desired box of interest. 1. Press the Zoom button to start HD Zoom. 2. Press the Select button and adjust the box so that it is as wide as possible, covering the left and right side of the image. Then make the box as thin as possible in the up-down direction. 3. Press the Select button again to move the box position. Move the box all the way on top of the screen. 4. Press the Select button again to adjust box size. Scroll down on the trackpad to lengthen the box size down. Scroll down so that the line reaches close to 1.5 cm. Be careful not to move the trackball up—doing so will cause the box to shrink from both the top and bottom side. If this happens, go back to step 2. 5. Press the Zoom knob again to enter an HD Zoom view.
Dynamic Range	50 dB	A dynamic range of 50 dB, the lowest allowable setting, helps make the image brighter. Ultimately this setting is not crucial and is more of a

		preference. However, the higher dynamic range tends to yield darker images, which could make image processing more difficult. If DIC is used in the future, this setting could help.
SuperRes	1	"SuperRes" is a setting that can improve image textures by reducing speckles. However, ultrasound speckles are still desired for speckle tracking in DIC. SuperRes setting has four settings; the setting values are integers that range from 0 to 4. A higher SuperRes value improves the image texture and reduces speckles. A SuperRes value of 1 was chosen. A value of 0 would have given the best speckle images, but a value of 1 helps ensure the image quality is still acceptable; this is important for analyzing ultrasound images without DIC. However, it should be noted that, subjectively, the images at different SuperRes settings did not seem to differ significantly. SuperRes is a setting that does not affect Frame Rate.

APPENDIX B: LABVIEW INSTRUCTIONS FOR LOAD CELL DATA COLLECTION

Conducting a trial with the LV software required the following hardware (this is strictly for the LV portion of the test, not the ultrasound imaging):

- Laptop with LV 2017 (32-bit)
- cDAQ-9178 with
    - NI 9237 C-series module with a D-Sub connector (x1)
    - Honeywell Subminiature Load Cell Model 13 (x4)

The following are instructions to run the LV code to collect the load cells' force data. The instructions are based on the specific hardware/software available at the VA Puget Sound.

1. Ensure the four miniature load cells are connected to the NI 9237 module.
2. Connect the NI 9237 to the cDAQ -9178 in slot 8 (the other slots or occupied by other C-series modules for another project).
3. Supply the cDAQ with power.
4. Connect the cDAQ's USB to the laptop with LV 2017 (the LV/CompactDAQ laptop).
5. Turn on the LV laptop.
    a. Connecting the cDAQ to the laptop will usually open the NI MAX application. It is safe to close this window.
6. Open the LV 2017 software.
7. Open the UltrasoundShoe_DAQ.lvprj
8. Open the UIMain.vi file that is within the UltrasoundShoe_DAQ project folder.
9. Run the UIMain.vi application by pressing the white arrow near the top of the window.

10. Zero the four load cells that are connected to the system. This may take several tries to get the running average as close to zero as possible. It is good to aim to be within 0.5 N of zero.
11. Select the filepath that the data will save in.
12. When the trial is ready to begin, press the {record} button on the user interface.
13. When the trial is complete, press the {stop} button on the user interface.
14. To collect more data, repeat steps 10-13 as many times as needed.
15. While data is not being collected, it is possible to load a data set. Do this by selecting the filepath to load, and the force data will populate the LV graph.
16. Once data collection is complete, ensure all data is properly saved and stop the VI from running. It is now safe to close the LV windows application.

APPENDIX C: ADDITIONAL INFORMATION ON ULTRASOUND VALIDATION TEST

The following are quality assurance images of the Gammex RMI 404GS LE phantom, captured by the SLH20-6 probe (Figure C1 – Figure C6).

Figure C1. Ultrasound image used for the vertical/horizontal distance check. Captured with the stock SLH20-6 probe.

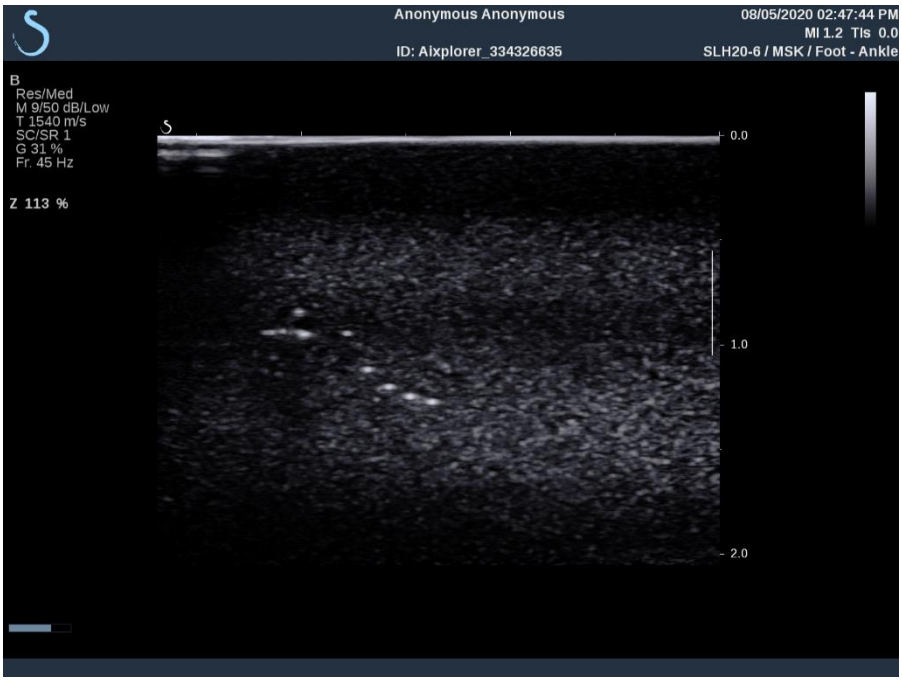

Figure C2. Ultrasound image used for the lateral/axial resolution check. Captured with the stock SLH20-6 probe.

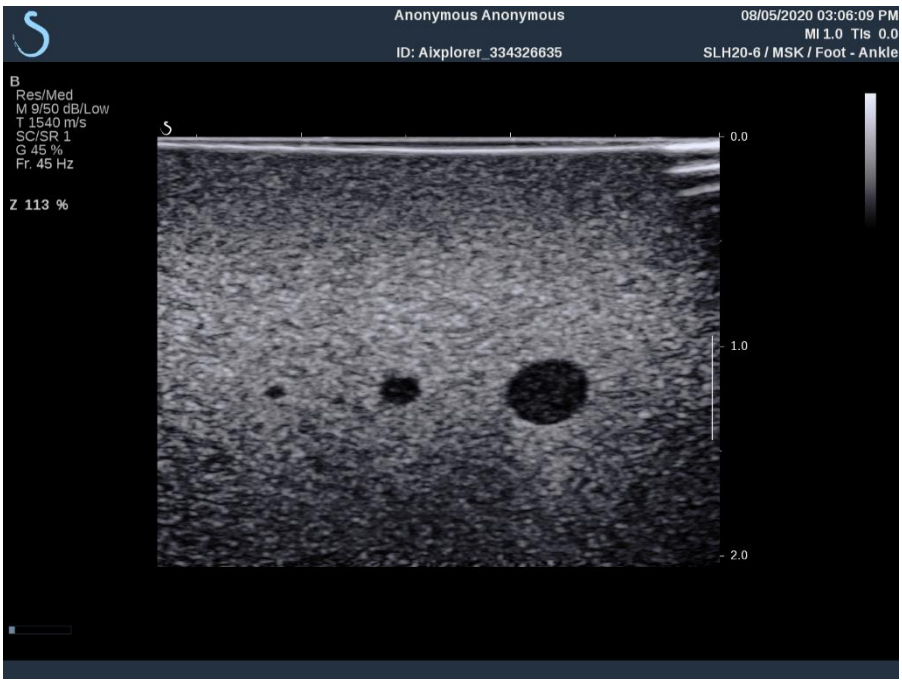

Figure C3. Ultrasound image used for the geometric check. Captured with the stock SLH20-6 probe.

Figure C4. Ultrasound image used for the vertical/horizontal distance check. Captured with the custom SLH20-6 probe.

Figure C5. Ultrasound image used for the lateral/axial distance check. Captured with the custom SLH20-6 probe.

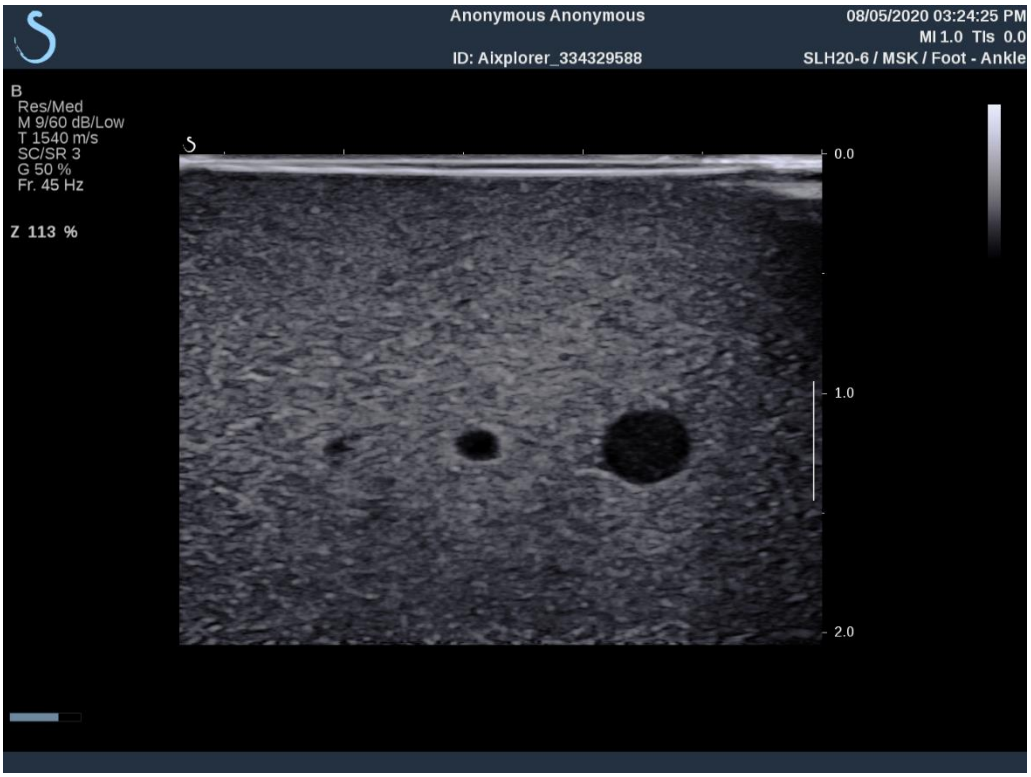

Figure C6. Ultrasound image used for the geometric check. Captured with the custom SLH20-6 probe.

The vertical and horizontal distance checks had more than a single sample. For vertical distance, the depth check began at the mark starting around 1 cm deep. The horizontal checks only looked at the three horizontal marks captured in the image (Table C1).

Table C1. Results of the distance checks. Vertical checks start at the vertical mark at about 1 cm and goes down from there. Horizontal checks start at the leftmost horizontal mark. Vertical and horizontal sample numbers are independent of each other.

Sample	Vertical distance (stock) [mm]	Vertical distance (custom) [mm]	Horizontal distance (stock) [mm]	Horizontal distance (custom) [mm]
1	4.42	4.42	9.68	9.68
2	5.83	5.83	9.74	10.19
3	4.81	4.81		
4	4.81	4.81		
5	4.81	4.81		
6	4.87	4.81		
7	4.81	4.87		

APPENDIX D: STATIC TEST RESULTS

The following are individual results from the static validation tests conducted on the load cells (Table D1 – Table D8).

Table D1. Static validation test - basic heel.

	Target 5 lbf	Target 10 lbf	Target 20 lbf
Trial 1	4.79	9.78	18.71
Trial 2	4.86	9.80	19.75
Trial 3	4.83	9.71	19.74
Trial 4	4.85	9.67	19.73
Trial 5	4.73	9.70	19.86
Average Error	3.79%	2.70%	1.21%

Table D2. Static validation test - basic forefoot.

	Target 5 lbf	Target 10 lbf	Target 20 lbf
Trial 1	4.83	9.84	19.68
Trial 2	4.68	9.81	19.64
Trial 3	4.84	9.87	19.61
Trial 4	4.73	9.74	19.72
Trial 5	4.80	9.70	19.66
Average Error	4.51%	2.09%	1.68%

Table D3. Static validation test - replica heel.

	Target 5 lbf	Target 10 lbf	Target 20 lbf
Trial 1	5.05	10.04	20.17
Trial 2	4.96	9.97	20.18
Trial 3	4.88	9.99	20.30
Average Error	1.39%	0.25%	1.09%

Table D4. Static validation test - replica forefoot.

	Target 5 lbf	Target 10 lbf	Target 20 lbf
Trial 1	4.91	9.90	19.99
Trial 2	5.07	9.84	20.15
Trial 3	4.96	9.92	20.07
Average Error	1.33%	1.17%	0.385%

Table D5. Static validation test - real heel.

	Target 5 lbf	Target 10 lbf	Target 20 lbf
Trial 1	5.03	9.96	19.89
Trial 2	4.92	9.88	20.27
Trial 3	4.84	9.94	20.27
Average Error	1.85%	0.74%	1.09%

Table D6. Static validation test - real forefoot.

	Target 5 lbf	Target 10 lbf	Target 20 lbf
Trial 1	4.98	10.01	20.28
Trial 2	5.01	10.19	20.14
Trial 3	4.92	9.85	20.01
Average Error	0.72%	1.15%	0.72%

Table D7. Static validation test - shoe table top heel.

	Target 5 lbf	Target 10 lbf	Target 20 lbf
Trial 1	4.98	9.71	19.22
Trial 2	4.94	9.80	19.70
Trial 3	4.84	9.85	19.67
Average Error	1.58%	2.12%	2.35%

Table D8. Static validation test - shoe table top forefoot.

	Target 5 lbf	Target 10 lbf	Target 20 lbf
Trial 1	5.00	9.92	19.71
Trial 2	4.81	9.76	19.46
Trial 3	4.82	9.96	19.75
Average Error	2.44%	1.20%	1.79%

APPENDIX E: RESOLUTION OF THE TEKSCAN SENSOR

The Tekscan 4201 sensor was used in tandem with the Tekscan software. The Tekscan software has a setting that allows the user to adjust the sensor's sensitivity. This was important to use because the 4201 sensor used was rated for 500 psi (3447 kPa). The sensitivity settings altered the sensor's saturation pressure—this value was determined by the Tekscan software.

Calculation of the force threshold:

Sensor matrix area: 21.1 mm x 45.7 mm (9.64 E-4 m^2)

Saturation pressure: 67.47 N/cm^2, or 647.7 kPa.

Res = 647.7 / 2^8 = 2.53 kPa

Minimum force that will be read by the sensor given the sensitivity setting:

Force = Pressure x Area

Force = 2.53 kPa x 9.64 E-4 m^2

Force = 2.44 N = 0.55 lbf

APPENDIX F: EXPLORING OPTIMAL INSOLE SHAPE AND WIDTH OF FORCE CONCENTRATOR FOR TESTING

The next static test was to add on the case covers. In doing so, the cutout shape of the insole and the force concentrator (FC) shape was investigated (Figure F1). Two trials were conducted to obtain the average result (Table F1).

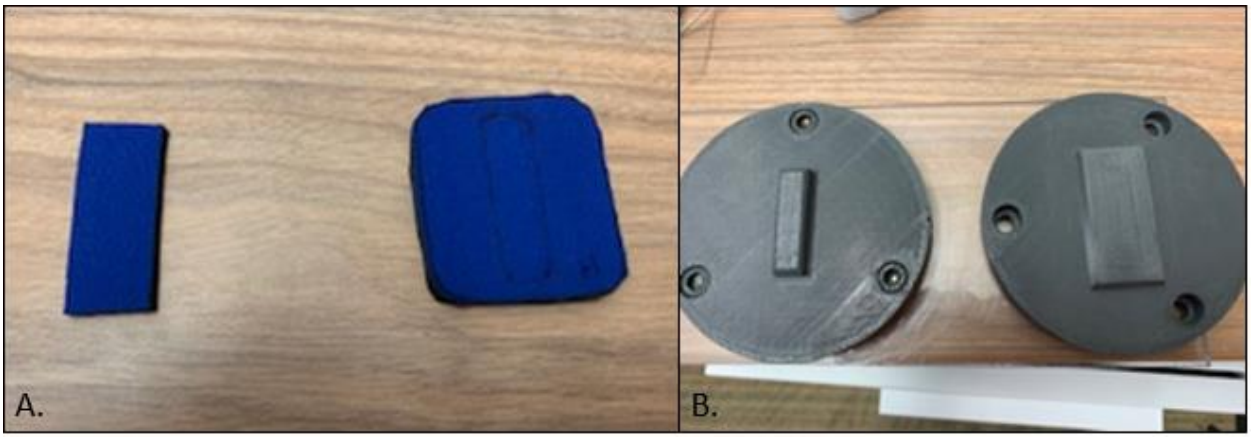

Figure F1. A) The wide insole (left) and narrow insole (right), still left inside a larger piece. B) Narrow force concentrator (left) and wide force concentrator (right).

Table F1. Testing different setups to determine best one to use for a static test prior to the final dynamic validation test.

Test Conditions	Weights	Load Cell [N]	LC error
FC-Wide Insole - Narrow	22.24 N	11.6	-43.7%
	44.48 N	21.3	-52.2%
	88.96 N	40.9	-54.1%
FC-Narrow Insole - Narrow	22.24 N	22.0	-1.08%
	44.48 N	42.1	-5.30%
	88.96 N	82.8	-6.99%
FC-Narrow Insole - Wide	22.24 N	21.1	-5.02%
	44.48 N	42.0	-5.58%
	88.96 N	83.5	-6.14%

After determining a wide force concentrator resulted in low accuracy, the next step was to conduct this test again with the Tekscan for the conditions that yielded reasonable accuracy. The configuration that appeared to be most accurate was then tested in the instrumented shoe. Load cell results shown were obtained from averaging two trials (Table F2).

Table F2. Another static test of different setups prior to the dynamic validation test. This static test includes a test inside the shoe.

Test Cond.	Weights	Load Cell [N]	Tekscan [N]	LC error	TS error
FC-Narrow Insole-Narrow Table top	22.24 N	20.0	11.5	-10.1%	-48.3%
	44.48 N	41.0	35.8	-7.83%	-19.6%
	88.96 N	80.1	84.0	-9.94%	-5.58%
FC-Narrow Insole-Wide Table top	22.24 N	22.1	9.50	-0.52%	-57.3%
	44.48 N	43.3	34.5	-2.77%	-22.4%
	88.96 N	85.0	90.0	-4.46%	1.16%
FC-Narrow Insole-Narrow In shoe	22.24 N	21.4	8.88	-3.89%	-60.1%
	44.48 N	41.3	30.5	-7.27%	-31.4%
	88.96 N	80.8	84.0	-9.23%	-5.58%